Modeling the Formation and Composition of Secondary Organic Aerosol from Diesel Exhaust Using Parameterized and Semi-Explicit Chemistry and Thermodynamic Models

Sailaja Eluri[1], Christopher D. Cappa[2], Beth Friedman[3], Delphine K. Farmer[3], and Shantanu H. Jathar[1]

[1] Department of Mechanical Engineering, Colorado State University, Fort Collins, CO, USA, 80523

[2] Department of Civil and Environmental Engineering, University of California Davis, Davis, CA, USA, 95616

[3] Department of Chemistry, Colorado State University, Fort Collins, CO, USA, 80523

Correspondence to: Shantanu H. Jathar (shantanu.jathar@colostate.edu)

Abstract

Laboratory-based studies have shown that combustion sources emit volatile organic compounds that can be photo-oxidized in the atmosphere to form secondary organic aerosol (SOA). In some cases, this SOA can exceed direct emissions of primary organic aerosol (POA). Jathar et al. (2017) recently reported on experiments that used an oxidation flow reactor (OFR) to measure the photochemical production of SOA from a diesel engine operated at two different engine loads (idle, load), two fuel types (diesel, biodiesel) and two aftertreatment configurations (with and without an oxidation catalyst and particle filter). In this work, we used two different SOA models, the volatility basis set (VBS) model and the statistical oxidation model (SOM), to simulate the formation and composition of SOA for those experiments. Leveraging recent laboratory-based parameterizations, both frameworks accounted for a semi-volatile and reactive POA; SOA production from semi-volatile, intermediate-volatility, and volatile organic compounds (SVOC, IVOC and VOC); NO_X-dependent parameterizations, multigenerational gas-phase chemistry; and kinetic gas/particle partitioning. Both frameworks demonstrated that for model predictions of SOA mass to agree with measurements across all engine load-fuel-aftertreatment combinations, it was necessary to model the kinetically-limited gas-particle partitioning in OFRs as well as account for SOA formation from IVOCs, which were on average found to account for 70% of the model-predicted SOA. Accounting for IVOCs however resulted in an average under-prediction of 28% for OA atomic O:C ratios. Model predictions of the gas-phase organic compounds (resolved in carbon and oxygen space) from the SOM compared favorably to gas-phase measurements from a Chemical Ionization Mass Spectrometer (CIMS), substantiating the semi-explicit chemistry captured by the SOM. Model-measurement comparisons were improved on using vapor wall-loss corrected SOA parameterizations. As OFRs are increasingly used to study SOA formation and evolution in laboratory and field environments, models such as those developed in this work can be used to interpret the OFR data.

1 Introduction

Combustion-related aerosols are an important contributor to urban and global air pollution and have impacts on climate (Pachauri et al., 2014) and human health (Anderson et al., 2012). While direct particle emissions from combustion sources are dominated by primary organic aerosol (POA) and black carbon (Bond et al., 2004), these sources also emit more volatile organic compounds (VOCs) that can photochemically react in the atmosphere to form secondary organic aerosol (SOA) (Robinson et al., 2007). SOA production from combustion emissions is poorly understood and not very well represented in models in terms of its precursors, gas-particle partitioning, composition, and properties (Fuzzi et al., 2015). Atmospheric models frequently under-predict SOA mass concentrations during strong photochemical episodes in urban areas (Jathar et al., 2017b), which likely highlights the challenge in modeling the SOA contributions from urban, combustion-related emissions (Ensberg et al., 2014).

Diesel-powered sources, which are an important source of air pollution at urban and regional scales, emit precursors that form SOA in the atmosphere (Gentner et al., 2016). Robinson et al. (2007) found that photochemical processing of exhaust emissions from a small off-road diesel engine led to SOA production and doubled the primary aerosol mass over a few hours in an environmental chamber. Chirico et al. (2010) and Gordon et al. (2014) performed similar chamber experiments on tailpipe emissions from in-fleet, on-road diesel vehicles run on chassis dynamometers. Both found SOA production that was roughly consistent with the findings from Robinson et al. (2007). They additionally found that the use of aftertreatment devices (diesel oxidation catalysts and diesel particulate filters) substantially reduced SOA production (mimicking the reduction in primary aerosol emissions) but observed some SOA production during cold starts and/or regeneration events when the proper functioning of the aftertreatment devices was limited. Furthermore, Gordon et al. (2014) found negligible differences in the SOA formation between diesel and biodiesel fuel. To access longer equivalent photochemical aging timescales compared to typical chamber experiments, Tkacik et al. (2014) measured SOA formation using an oxidation flow reactor (OFR) from air sampled from a highway tunnel in Pittsburgh, PA used by both on-road gasoline and diesel vehicles. OFRs use high concentrations of atmospheric oxidants, e.g. hydroxyl radicals, to achieve long exposures on short actual timescales; further discussion is provided below. Tkacik et al. (2014) measured much stronger SOA formation compared to chambers (SOA: POA was 10:1) over photochemical exposures equivalent to 2 to 3 days, but found that the SOA was lost, or destroyed, as the mixture continued to age over the timescale of a week. Recently, Jathar et al. (2017a) performed experiments using an oxidation flow reactor to measure the photochemical production of SOA from an off-road diesel engine operated at various engine load, fuel, and aftertreatment configurations. Jathar et al.

69 [(2017a)](#) found that efficient combustion at higher engine loads and removal of SOA precursors by

70 aftertreatment systems reduced SOA production by factors of 2 to 10. The only exception was that the

71 aftertreatment system did not seem to reduce SOA production at idle loads possibly because the exhaust

72 temperatures were low enough to limit removal of SOA precursors in the oxidation catalyst. Overall,

73 these studies indicate that diesel exhaust contributes to atmospheric SOA production, although the precise

74 production of SOA varies across dimensions of photochemical age, engine duty cycle, use of alternative

75 fuels, and aftertreatment devices.

76

77 Oxidation flow reactors are being used to study the photochemical production of SOA from both

78 anthropogenic (e.g., [Ortega et al. (2016)](#)) and natural (e.g., [Palm et al. (2016)](#)) sources. Most OFRs used

79 for SOA studies are 10 to 15 L, flow-through metal reactors with lamps that can produce high

80 concentrations of atmospheric oxidants to simulate photochemical processing (e.g., [Lambe et al. (2011)](#)).

81 Flows through an OFR allow for residence times between one and four minutes, but given the high

82 oxidant concentrations OFRs can simulate several weeks of photochemistry. OFRs have three distinct

83 advantages over environmental chambers. First, OFRs are smaller in size and easier to operate than

84 environmental chambers, which allows for shorter experiments and makes them ideal for field

85 deployments ([Palm et al., 2016](#);[Simonen et al., 2017](#)). Second, production of high oxidant concentrations

86 in OFRs allows for much longer photochemical exposures (~factor of 10) than those possible with

87 chambers ([Lambe et al., 2011](#)). Third, due to their flow-through nature, OFRs have shorter residence

88 times than conventional chambers (~1-4 minutes) and hence are less susceptible to gas and particle losses

89 that can influence SOA formation ([Zhang et al., 2014](#);[Krechmer et al., 2016](#)). Despite those advantages,

90 there are concerns that the accelerated chemistry and limitations to gas/particle partitioning may affect the

91 formation and composition of SOA in OFRs, which calls into question their relevance in understanding

92 SOA formation in the real atmosphere ([Palm et al., 2016](#);[Jathar et al., 2017a](#);[Ahlberg et al., 2017](#)). For

93 example, short residence times and/or small condensation sinks from preexisting aerosol may not allow

94 for complete condensation of SOA vapors ([Lambe et al., 2015](#)). Similarly, high oxidant concentrations in

95 OFRs may lead to molecules undergoing a greater number of reactions in the gas-phase before

96 condensing, including reactions that lead to fragmentation and formation of higher volatility products

97 ([Kroll et al., 2009](#)). Both effects will typically suppress SOA production. With the increased use of OFRs,

98 there is a need to develop and use modeling tools that can account for fragmentation reactions and kinetic

99 gas/particle partitioning. This will allow for a more accurate interpretation of OFR data and facilitate

100 translation of OFR results to the real atmosphere.

101

102   Models used to simulate the photochemical production of SOA from VOCs in combustion emissions have

103   traditionally used the two-product (Odum et al., 1996) or the more generalized n-product volatility basis

104   set (VBS) framework (Donahue et al., 2006a). In this framework, VOC oxidation products are lumped

105   into volatility bins based on their effective saturation concentrations ($C*$) and where the saturation

106   concentration determines the partitioning of the products between the gas and particle phases (Pankow,

107   1994). This framework has been widely used in both box (Dzepina et al., 2009;Hodzic et al., 2010;Jathar

108   et al., 2014a;Hayes et al., 2015) and three-dimensional (Murphy and Pandis, 2009;Tsimpidi et al.,

109   2009;Jathar et al., 2011;Ahmadov et al., 2012;Konovalov et al., 2015) models to simulate the chemistry

110   and gas/particle partitioning of SOA. While this framework offers a simple and computationally efficient

111   scheme to model SOA formation, the use of volatility alone neither tracks the molecular composition, nor

112   informs the continued multi-generational chemistry that will determine the atmospheric evolution and

113   properties of SOA. As a result, volatility-based models have been challenged in leveraging observations

114   of the elemental composition of SOA (e.g., atomic O:C ratios) that have become possible through the use

115   of the aerosol mass spectrometer (AMS) to constrain parameterizations or test model predictions. Further,

116   most volatility-based models have employed *ad hoc* parameterizations to model multi-generational

117   chemistry that do not account for fragmentation reactions (Robinson et al., 2007) and possibly double

118   count SOA formation (Jathar et al., 2016). Therefore, there is a demand to develop models that can

119   provide an improved representation of the chemistry that governs the formation, composition, and

120   properties of SOA.

121

122   Previously, volatility-based SOA models have been used to predict photochemical production of SOA

123   from motor vehicle exhaust (Robinson et al., 2007;Jathar et al., 2014b;Tkacik et al., 2014). These

124   modeling studies have shown that speciated SOA precursors such as long alkanes (C_{6-12}) and single-ring

125   aromatics (e.g., benzene, toluene) explain less than 20% of the observed SOA and have argued that the

126   remainder of the SOA (~80%) arises from the photooxidation of typically unspeciated organic

127   compounds. These unspeciated compounds, also referred to as intermediate volatility organic compounds

128   (IVOCs), are likely species with carbon numbers larger than 12 and appear as an unresolved complex

129   mixture on using traditional gas chromatography mass spectrometry (GC-MS) techniques (Presto et al.,

130   2011). Early estimates of IVOC emissions and their SOA potential have significantly improved

131   predictions of the SOA formed from diesel exhaust (Jathar et al., 2014b) and have broadly improved OA

132   model performance in three-dimensional large-scale models (Murphy and Pandis, 2009;Pye and Seinfeld,

133   2010;Jathar et al., 2011;Tsimpidi et al., 2009). Consider as an example that Zhao et al. (2015), using a

134   thermal desorption GC-MS to provide detailed speciation of the carbon-number resolved linear, branched,

4

and cyclic alkane IVOCs in diesel exhaust, found that these species accounted for up to 60% of the non-methane organic gas emissions. While IVOCs have been recognized as an important class of SOA precursors for diesel (and even for gasoline and biomass burning) sources, updated emissions and speciation estimates from Zhao et al. (2015) have not yet been used to explain observations of photochemically produced SOA from diesel exhaust.

Recently, several model frameworks have been developed to improve the representation of SOA formation, considering dimensions of SOA beyond just volatility. The statistical oxidation model (SOM) developed by Cappa and Wilson (2012) is one such example, although volatility remains an important consideration. The SOM is a semi-explicit, parameterizable mechanism that uses a two-dimensional carbon-oxygen grid to simulate the multigenerational chemistry and gas/particle partitioning of organic compounds. Although the SOM does not explicitly track or specify the product species composition (e.g., functional groups), the carbon- and oxygen-number representation provides adequate detail to represent many key atmospheric processes, e.g., reactions with oxidants, formation of functionalized products, scission of carbon backbones or fragmentation, surface and condensed-phase chemistry and gas/particle partitioning. The SOM has been used to interpret chamber experiments (Zhang et al., 2014;Cappa et al., 2013;Cappa and Wilson, 2012) and was recently integrated into a chemical transport model (Jathar et al., 2015) to examine the influence of multigenerational aging (Jathar et al., 2016) and chamber-based vapor wall losses (Cappa et al., 2016) on ambient concentrations and properties of OA. The two-dimensional VBS (2D-VBS) of Donahue et al. (2011) and the carbon-polarity grid of Pankow and Barsanti (2009) are examples of similar frameworks. These more sophisticated models (i.e., SOM, 2D-VBS, carbon-polarity grid) have not yet been employed to study SOA formation from complex mixtures such as combustion emissions.

To summarize, combustion sources such as diesel-powered sources emit precursors that can photooxidize in the atmosphere to produce SOA. This SOA production is dependent not only on the precursor composition (that could vary by combustion mode and fuel type) and photochemical age, but also experimental artifacts (e.g., short condensation timescales) introduced by oxidation flow reactors. Hence, there is a need to develop and apply sophisticated, yet computationally efficient, numerical models to simulate and study SOA formation from combustion emissions. In this work, we applied two SOA model frameworks that vary in sophistication (VBS and SOM) to simulate the photochemical production of SOA in an OFR from diesel exhaust. The models were evaluated by comparing model predictions (OA and O:C) to the recent measurements made by Jathar et al. (2017a) where SOA production was quantified for

168 different photochemical ages under varying engine loads, fuels, and aftertreatment devices. The model-

169 measurement comparison, along with sensitivity simulations, highlights the importance of modeling the

170 kinetic gas/particle partitioning of SOA in OFRs, the contribution of IVOCs to the total SOA production,

171 and the ability of the SOM to accurately track the composition of SOA.

172

173 **2 Methods**

174 **2.1 Experiments and Data**

175 Jathar et al. (2017a) performed photooxidation experiments using an OFR to measure SOA production

176 from the exhaust of a 4.5L, John Deere diesel engine. The stock engine met Tier 3 emissions standards for

177 off-road diesel engines. The OFR used therein was described in detail by Friedman et al. (2016) and the

178 experimental setup and OA measurements from these experiments were described in detail by Jathar et al.

179 (2017a). We briefly summarize the experimental setup, measurements, and findings from Jathar et al.

180 (2017a). The engine was run at two different loads (idle and 50% load) with two different fuels (diesel

181 and biodiesel), and with and without an aftertreatment system. The aftertreatment system included a diesel

182 oxidation catalyst (DOC) to oxidize CO and THC and a diesel particle filter (DPF) to trap fine particles.

183 Diesel exhaust was diluted by a factor of 45-110 before entering the OFR. The intensity of the mercury

184 lamps (at wavelengths of 185 and 254 nm) inside the OFR was varied to produce different hydroxyl

185 radical (OH) concentrations and simulate different photochemical exposures. The OFR had a residence

186 time of 100 s. A suite of instrumentation was used to measure gas- (CO_2, CO, total hydrocarbons, NO_x,

187 O_2, oxygenated organic compounds) and particle- (aerosol size and composition) phase concentrations. A

188 total of fourteen experiments (see Table 1 for more details) were performed at varying engine loads and

189 with varying fuels and aftertreatment configurations. The OH exposure was varied between 0 and a

190 maximum of 9.2×10^7 molecules-hr cm^{-3} (equivalent to 2 days of photochemical aging at an OH

191 concentration of 1.5×10^6 molecules cm^{-3}). On average, each experiment included measurements at six to

192 seven different photochemical exposures. The mass concentrations and elemental composition of the POA

193 (measured when OFR lights were off) and SOA (at varying OH exposures) were measured by a high-

194 resolution aerosol mass spectrometer (HR-AMS). In addition to the measurements reported by Jathar et al.

195 (2017a), the gas-phase concentrations of oxygenated organic compounds were measured by an acetate

196 reagent ion-based chemical ionization mass spectrometer (CIMS) (Link et al., 2016). At all engine

197 configurations, SOA production exceeded the POA emissions after the equivalent of a few hours of

198 atmospheric photochemical aging. SOA production was particularly strong at idle (or less fuel-efficient)

199 engine loads and/or when exhaust temperatures were low and proper functioning of the aftertreatment

200 devices was limited. Further, POA emissions and SOA production were nearly identical between diesel

6

201 and biodiesel fuels. A synopsis of experiments performed and the total hydrocarbons (THC), which

202 includes all SOA precursors, POA, SOA, O:C, OH, and size distribution data are presented in Table 1.

203

204 Although the diesel exhaust was diluted with clean air to produce atmospherically-relevant concentrations

205 of POA, the initial THC, CO, and NO_X concentrations in the OFR were still quite high. Peng and Jimenez

206 (2017), using a detailed gas-phase model, argued that the high external OH reactivity from high THC,

207 CO, and NO_X concentrations might lead to non-OH chemistry in the OFR and NO could quickly be

208 consumed in the OFR leading to low NO conditions for SOA formation. Peng and Jimenez (2017)

209 quantified the potential influence of NO on the oxidation chemistry by calculating the ratio of the reactive

210 flux of the peroxy radicals with NO to the reactive flux of the peroxy radicals with HO_2 ($r_{RO2+NO}/r_{RO2+HO2)}$.

211 A ratio greater than 1 was considered as "high NO" while a ratio less than 1 was considered "low NO".

212 For the relative humidity, photon flux, initial NO, and external OH reactivity values in Jathar et al.

213 (2017a), the model of Peng and Jimenez (2017) predicted that the OFR mostly ran in a high NO mode at

214 all photochemical exposures when the engine was run at load conditions or with an aftertreatment device

215 in place. However, the model predicted that the OFR mostly ran in a low NO mode especially at the high

216 photochemical exposures when the engine was run at idle conditions and without an aftertreatment device

217 (i.e., Idle-Diesel-None and Idle-Biodiesel-None). The $r_{RO2+NO}/r_{RO2+HO2}$ ratio and low versus high NO

218 mode for each photon flux-experiment combination is listed in Table S1. Based on these results, we

219 accordingly used the low and high NO_X parameterizations to perform the model simulations.

220

221 The model of Peng and Jimenez (2017) also indicated that most of the experiments performed by Jathar et

222 al. (2017) were run under, in what Peng and Jimenez (2017) refer to as, 'risky' or 'bad' conditions. These

223 conditions refer to situations in the OFR where the initial NO concentrations and external OH reactivity

224 are high enough to suppress OH exposure and lead to non-tropospheric photolysis at 185 and 254 nm,

225 which could compete with OH exposure to determine the fate of the SOA precursors and its oxidation

226 products. Such conditions could be avoided by ensuring low initial NO concentrations and external OH

227 reactivity that for combustion emissions would require substantial dilution with clean air before they are

228 oxidized in the OFR. Future studies on combustion sources should be cognizant of this fact to avoid

229 artifacts linked to non-tropospheric photolysis of organic compounds in OFRs.

230

231 **2.2 Organic Aerosol Models**

232 In this work, we used two different OA models to predict the mass concentrations and chemical

233 composition of SOA and compare predictions against the SOA measurements from Jathar et al. (2017a)

234   and Friedman et al. (2017). In this section, we briefly describe the two model frameworks, namely the

235   Volatility Basis Set (VBS) and the Statistical Oxidation Model (SOM), used to simulate the coupled

236   chemistry, thermodynamic properties, and kinetic gas/particle partitioning of OA. Neither model

237   accounted for photolysis of organic compounds in the gas phase at 185 or 254 nm, which may need to be

238   considered in the future when modeling the OFR chemistry from combustion emissions. The VBS model

239   was chosen as it is widely used in contemporary air quality models; the SOM was chosen to examine the

240   influence of improved representation of OA processes (e.g., fragmentation reactions) on model

241   predictions.

242

243   **2.2.1 Volatility Basis Set**

244   The Volatility Basis Set model, developed by Donahue et al. (2006b), is a parameterizable model that

245   allows for a volatility-based representation of the coupled chemistry, thermodynamic properties, and

246   gas/particle partitioning of OA. The VBS uses logarithmically spaced so-called basis sets based on the

247   effective saturation concentration (C^*); C^* of a species determines the partitioning between the gas and

248   particle phases (Pankow, 1994). In the VBS model, organic precursors were allowed to react with OH to

249   yield a unique product distribution in C^* space that represented stable first-generation products.

250   Subsequent multi-generational gas-phase oxidation, or so-called 'aging,' of the VBS products was

251   modeled using the scheme of Robinson et al. (2007). In this scheme the product species are allowed to

252   react with OH and yield a product with a C^* that is an order of magnitude lower than the direct precursor,

253   to a lower limit C^* of 10^{-2} µg m^{-3}. This scheme did not consider fragmentation reactions. The following

254   equations were used to represent the organic precursor oxidation (equation 1) and subsequent reaction and

255   formation of products from the precursor oxidation and aging reactions (equation 2):

256    $$\frac{dV}{dt} = -k_{OH}[V][OH] \tag{1}$$

257    $$\frac{dC_j^{g+p}}{dt} = \alpha_j k_{OH}[V][OH] + \beta\, k_{OH,aging}[C_{j+1}^g][OH] - \gamma\, k_{OH,aging}[C_j^g][OH] \tag{2}$$

258   where V is the gas-phase concentration of a generic organic precursor (µg m^{-3}; includes VOCs, IVOCs

259   and SVOCs), k_{OH} is the reaction rate constant between the precursor and OH (cm^3 molecule^{-1} s^{-1}), C_j^{g+p}

260   is the gas + particle-phase concentration in the jth bin (µg m^{-3}), α_j is the mass yield of the first-generation

261   oxidation product of the jth bin (Table 2), $k_{OH,aging}$ is the reaction rate constant (cm^3 molecule^{-1} s^{-1}) to

262   represent multi-generational aging of the oxidation products, and β and γ are the mass yields associated

263   with the production and loss terms from multi-generational aging. For the jth bin, the second term in

264   equation (2) represents the formation of oxidation products from the $j+1^{th}$ volatility bin and the third term

265   in equation (2) represents the loss of precursor from the jth bin. β and γ are assumed to have a value of 1

266   (meaning no fragmentation) but β is zero for the last bin and γ is zero for the first bin.

267

268   Volatility-resolved mass yields for eighteen different organic precursors for C^* bins ranging from 10^{-1} to

269   10^3 µg m^{-3} were adopted or refit based on low and high NO$_X$ parameterizations published in the literature;

270   organic precursors, the high and low NO$_X$ VBS mass yields, and the relevant references are listed in

271   Tables 2 and 3. Since there were no direct low NO$_X$ VBS parameterizations for alkanes, parameterizations

272   for linear, branched, and cyclic alkanes were developed using pseudo chamber data generated with the

273   SOM based on the low NO$_X$ parameters listed in Table 5 for *n*-dodecane, methylundecane, and

274   hexylcyclohexane respectively. Some of these parameterizations accounted for vapor wall losses and have

275   been accordingly marked in Tables 2 and 3. Each SOA precursor in the exhaust emissions was assigned a

276   surrogate from Table 2/3 to model SOA formation in the VBS model. When using the high NO$_X$

277   parameterizations, branched and cyclic alkanes were assigned surrogates based on equivalent linear

278   alkanes, following the work of Lim and Ziemann (2009) and Tkacik et al. (2012). A C$_X$ branched alkane

279   was assigned a C$_{X-2}$ linear alkane as a surrogate and a C$_X$ cyclic alkane was assigned a C$_{X+2}$ linear alkane

280   as a surrogate. Since we only fit alkanes up to *n*-heptadecane, we considered *n*-heptadecane as a surrogate

281   for alkanes C$_{17}$-C$_{22}$. The Idle-Diesel-None and Idle-Biodiesel-None experiments used the low NO$_X$

282   parameterizations while all the other experiments used the high NO$_X$ parameterizations. The mass transfer

283   (condensation/evaporation) of the VBS products to the particle phase was assumed to be kinetically-

284   limited in the OFR (Palm et al., 2016;Jathar et al., 2017a;Ahlberg et al., 2017); Section 2.3 describes the

285   mass transfer equation used to model kinetic gas/particle partitioning.

286

287   **2.2.2 Statistical Oxidation Model**

288   The Statistical Oxidation Model (SOM), developed by Cappa and Wilson (2012) is a semi-explicit,

289   parameterizable model that allows for a statistical representation of the coupled chemistry,

290   thermodynamic properties, and gas/particle partitioning of OA. The SOM uses a 2-dimensional carbon-

291   oxygen grid to track gas- and particle-phase precursors and products from precursor oxidation. Each cell

292   in the SOM grid represents a model organic species with a molecular weight defined by the formula

293      $C_xH_yO_z$. A SOM species reflects the average properties (e.g. C^*, reactivity) of all actual species with the

294   same number of carbon (N_C) and oxygen (N_O) atoms that are produced from a given precursor class (e.g.,

295   benzene, alkanes). In the SOM, all gas-phase species are assumed to be reactive towards OH and the OH

296   reaction rate constant (k_{OH}) is calculated using equation 3 as follows:

297 $$log(k_{OH}) = A_1 + A_2 \times (N_C^{A_3}) \times exp(-1 \times \frac{E_a}{8.314 \times T}) \times [1 + \frac{b_1}{\sigma\sqrt{2\pi}} exp(-\frac{1(ln(N_O+0.01)-ln(b_2)^2}{2\sigma^2})] \quad (3)$$

298 $\sigma (N_C \leq 15) = 0.0214 \times N_C + 0.5238$

299 $\sigma (N_C \geq 15) = -0.115 \times N_C + 2.695$

300 $b_1 = -0.2583 \times N_C + 5.8944$

301 $b_2 (N_C \leq 15) = 0.0314 \times N_C + 0.9871; \; b_2 (N_C > 15) = 0.25 \times N_C - 2.183$

302 where A_1=15.1, A_2=3.94, and A_3=0.797. k_{OH} for a specified N_C and N_O is assumed to be the same for

303 species in all the SOM grids.

304

305 The reactions with OH lead to either functionalization or fragmentation, resulting in movement through

306 the carbon-oxygen grid. Six precursor-specific adjustable parameters are assigned for each SOM grid:

307 four parameters that define the molar yields of the four functionalized, oxidized products ($p_{O,k}$, $\Sigma p_{O,k}$=1

308 and hence one out of the four parameters is determined by mass balance), one parameter that determines

309 the probability of functionalization or fragmentation (P_{Frag}, P_{Func}=1-P_{Frag}) and one parameter that

310 describes the change in C^* associated with the addition of one oxygen atom (ΔLVP). Equation 4

311 represents the evolution of species in the SOM grid:

312 $$\frac{d[C_XO_Z]}{dt} = -k_{OH}^{X,Z}[OH][C_XO_Z] + [OH]\sum_{k=1}^{4} k_{OH}^{X,Z-k} P_{func}^{X,Z-k} p_{O,k}[C_XO_{Z-k}] +$$

313 $$[OH]\sum_{j=1}^{jmax}\sum_{k=0}^{kmax-Z} k_{OH}^{X+j,Z-1+k} \frac{P_{frag}^{X,Z-1+k}}{N_{fragments}^{X,Z}}[C_XO_{Z-1+k}] \quad (4)$$

314 where C_XO_Z is the gas + particle-phase concentration of the SOM species with X carbon atoms and Z

315 oxygen atoms (μg m^{-3}) and $N_{fragments}$ is the number of possible products from fragmentation. The

316 probability of fragmentation is modeled using equation 5 as a function of the O:C ratio because higher

317 O:C ratio compounds are expected to have a higher probability of fragmentation (Chacon-Madrid and

318 Donahue, 2011):

319 $$P_{frag} = (\frac{N_O}{N_C})^{m_{frag}} \quad (5)$$

320 The C^* for each SOM species was calculated using equation 6 as follows:

321 $$log_{10}C^* = -0.337MW_{HC} + 11.56 - (N_O \times \Delta LVP) \quad (6)$$

322 where MW_{HC} (g mole^{-1}) is the molecular weight of the hydrocarbon backbone (accounting only for the

323 carbon and hydrogen atoms).

324

325 The parameters used to model SOA formation were based on those published in Cappa et al. (2016) and

326 are listed in Tables 4 and 5. These parameter sets were developed by fitting the SOM predictions to

327   chamber measurements of SOA mass concentrations and include corrections to account for vapor wall

328   losses (Zhang et al., 2014). Each SOA precursor in the exhaust emissions was assigned a surrogate from

329   Table 4 or 5 to account for the oxidation chemistry associated with oxidation of that species. For example,

330   pentadecane used the parameterization developed by fitting n-dodecane. The difference in the initial

331   number of carbons and oxygens, and thus the volatility, between the surrogate compound and the

332   precursor compound of interest was accounted for, with consequent impact on the SOA yield. In other

333   words, unlike the VBS where the SOA mass yield of the SOA precursor and surrogate is identical, the

334   surrogate in the SOM only informed the statistical trajectory for multi-generational oxidation of a given

335   precursor, and the surrogate and actual compound of interest can have different SOA mass yields. The

336   Idle-Diesel-None and Idle-Biodiesel-None experiments used the low NO_X parameters while all the other

337   experiments used the high NO_X parameters. Similar to the VBS model, the mass transfer

338   (condensation/evaporation) of the SOM products to the particle phase was assumed to be kinetically-

339   limited in the OFR (Palm et al., 2016;Jathar et al., 2017a;Ahlberg et al., 2017) and Section 2.3 below

340   describes the mass transfer equation used to model kinetic gas/particle partitioning.

341

342   **2.3 Kinetic Gas/Particle Partitioning**

343   Palm et al. (2016), (Ahlberg et al., 2017), and Jathar et al. (2017a) have argued that the short residence

344   times and small condensation sinks in the OFR may not permit all low-volatility products formed from

345   precursor oxidation to condense onto preexisting aerosol. Hence, unlike earlier work that has assumed

346   equilibrium partitioning to model SOA in OFRs (Tkacik et al., 2014;Chen et al., 2013), we modeled the

347   kinetic gas/particle partitioning of OA using equation 7 (Zhang et al., 2014):

348   $$\frac{dc_i^p}{dt} = 2\pi D_i D_p N_p F_{FS}\left(C_i^g - \frac{c_i^p C_i^*}{C_{OA}}\right) \qquad (7)$$

349   where C_i^p is the particle-phase mass concentration for the ith organic species (µg m^{-3}), D_i is the gas-phase

350   diffusion coefficient of the ith organic species (m^2 s^{-1}), D_p is the number mean particle diameter (m) , N_p is

351   the total particle number concentration (m^{-3}), F_{FS} is Fuchs-Sutugin correction for non-continuum mass

352   transfer, C_i^g is the gas-phase mass concentration of the ith organic species (µg m^{-3}), C_i^* is the effective

353   saturation concentration of the ith organic species, and C_{OA} is the total OA mass concentration (µg m^{-3}).

354   The ith organic species refers to the organic compounds tracked in the VBS bins and the SOM grids. The

355   gas-phase diffusion coefficient was calculated for each organic species as follows:

356   $$D_i = D_{CO_2} \frac{MW_{CO_2}}{MW_i} \qquad (8)$$

357   where D_{CO_2} is the gas-phase diffusion coefficient of CO_2 (1.38×10^{-5} m^2 s^{-1}), MW_{CO_2} (g mole^{-1}) is the

358 molecular weight of CO_2, and MW_i (g mole^{-1}) is the molecular weight of the ith organic species. In the

359 VBS model where we do not track the molecular composition of the SOA species, we assumed all

360 condensing species to have a molecular weight of 200 g mole^{-1}. This formulation to calculate the gas-

361 phase diffusion coefficient under-predicted the measured gas-phase diffusion coefficients compiled by

362 Tang et al. (2015) by ~20%. However, doubling the gas-phase diffusion coefficient calculated in equation

363 8 resulted in very small change (<1%) in the OA mass predictions for a representative experiment. Hence,

364 we decided to use the formulation in equation (8) for the rest of this work. The Fuchs-Sutugin correction

365 was calculated as follows:

366 $$F_{FS} = \frac{0.75\alpha(1+Kn)}{Kn^2 + Kn + 0.283 \cdot Kn \cdot \alpha + 0.75\alpha} \tag{9}$$

367 $$Kn = \frac{2\lambda_i}{D_p} \tag{10}$$

368 $$\lambda_i = \frac{3D_i}{C_j} \tag{11}$$

369 $$C_i = \sqrt{\frac{8N_A kT}{\pi MW_i}} \tag{12}$$

370 where Kn is the Knudsen number, α is the mass accommodation coefficient, λ_i is the mean free path of the

371 i^{th} organic species in air (m), C_i is the root mean square speed of the gas (m s^{-1}), N_A is Avogadro's number

372 (molecules mole^{-1}), k is the Boltzmann constant (m^2 kg s^{-2} K^{-1}), and T is the temperature (K).

373

374 **2.4 Model Inputs**

375 **2.4.1 Semi-Volatile and Reactive POA**

376 Previous work has shown that much of combustion-related POA is semi-volatile and exists in an

377 equilibrium with gas-phase vapors (Robinson et al., 2007;Huffman et al., 2009;May et al., 2013c, b;May

378 et al., 2013a). Jathar et al. (2017a) measured emissions of POA at no OH exposure and these measured

379 concentrations were used to initialize the seed OA available for partitioning in the OFR and to calculate

380 the mass concentrations of vapors in equilibrium with the POA. The mass concentrations of the POA

381 vapors were determined based on the normalized, volatility-resolved distribution of primary organic

382 compounds estimated by May et al. (2013b) for emissions from a suite of on- and off-road diesel vehicles.

383 The volatility distribution of May et al. (2013b) for diesel primary organic compounds is listed in Table

384 6(a). For the SOM, we assumed that the primary organic compounds could be represented using a

385 distribution of *n*-alkanes and we refit the volatility distribution in Table 6(a) to develop a carbon-number

386 resolved distribution of *n*-alkanes; this distribution is listed in Table 6(b).

387

2.4.2 SOA Precursors

388

389　Jathar et al. (2017a) did not speciate the THC or SOA precursor emissions from the diesel engine and

390　hence we have developed our own emissions profiles based on previously published literature to speciate

391　the THC emissions. In this work, we used two different emissions profiles listed in EPA SPECIATE

392　version 4.3 that are commonly used to speciate THC emissions from diesel engines for emissions

393　inventories used in atmospheric modeling (EPA, 2013): Profiles #3161 (Diesel Exhaust- Farm

394　Equipment) and #8774 (Heavy Duty Diesel Exhaust). Profile #3161 best matched the diesel engine source

395　and diesel fuel used by Jathar et al. (2017a) and was used as the baseline emissions profile to speciate the

396　THC emissions; we examined the sensitivity of using Profile #8774 on model predictions. We were

397　unable to find a comprehensive emissions profile for THC emissions from the use of straight biodiesel

398　fuel in the literature, and have relied on emissions profiles that were determined for biodiesel-diesel

399　blends. Profile #4777 (30% Biodiesel Exhaust - Light Duty) was used as the baseline emissions profile to

400　speciate THC emissions for experiments performed using the biodiesel fuel. All three emissions profiles

401　(3161, 8774, and 4777) are listed in Tables S2 through S4.

402

403　Prior work in studying SOA formation has revealed that traditional speciation of THC emissions does not

404　include emissions of high molecular-weight organic compounds, such as IVOCs, that are important SOA

405　precursors (Jathar et al., 2014b). In Profile #3161 such compounds are partially accounted for in the

406　'unknown' species category (13.76% by mass of THC). Zhao et al. (2015) recently estimated that IVOCs

407　were 60% of the THC emissions from a suite of on- and off-road diesel engines and provided a semi-

408　explicit speciation of the IVOC emissions as a carbon-number distribution of linear, branched and cyclic

409　alkanes. To account for these IVOC emissions, we assumed that the base case emissions profiles

410　contained 30% IVOCs on a mass-basis (this IVOC fraction was selected since it resulted in the most

411　optimum model-measurement comparison for OA mass; this will be discussed later in Section 3.3) and

412　had the same chemical speciation as that proposed by Zhao et al. (2015) for an off-road engine

413　(transportation refrigeration unit). We performed sensitivity simulations using IVOC fractions of 0%

414　(assuming that the THC emissions contained no IVOCs), 13.76% (based on the 'unknown' category in

415　Profile #3161), and 60% (based on the median estimate in Zhao et al. (2015)), on a mass-basis. Addition

416　of IVOCs to the emissions profile meant that the VOC species (e.g. benzene, toluene, short alkanes) had

417　to be renormalized to accommodate the IVOCs. Table 7 lists the renormalized baseline emissions profiles

418　for SOA precursors used for diesel and biodiesel exhaust with 30% IVOCs along with the reaction rate

419　constants with OH (k_{OH}) and surrogates (or model compound) used to model SOA formation for the VBS

420　and SOM models. Concentrations for each species were determined by multiplying the experiment-

13

421   specific THC mass concentrations with the renormalized emissions profiles.

422

2.4.3 Particle Size and Particle Number Concentrations

424   For numerical simplicity, we used a monodisperse aerosol, the properties of which (number mean

425   diameter (D_p) and number concentration (N_p)) were initialized from the measured particle size distribution

426   data when modeling kinetic gas/particle partitioning. For experiments performed without the DPF+DOC,

427   the initial particle number concentrations and condensational sinks were high (>3.3×10^5 # cm^{-3} and >0.5

428   min^{-1}) and hence the monodisperse aerosol was initialized based on data at no photochemical exposure.

429   For experiments performed with the DPF+DOC where the initial particle number concentrations were

430   relatively low (<1000 # cm^{-3} and <0.003 min^{-1}), photochemical aging resulted in formation and growth of

431   new particles and provided a substantial increase in the surface area (>factor of 300) available for

432   condensation. In these experiments, we initialized the monodisperse aerosol using an average of the data

433   at no photochemical exposure and after photochemical exposure (Palm et al., 2016). Averaging the data

434   allowed for a more realistic estimate of the condensational sink. In each simulation, the condensing SOA

435   mass was used to calculate the change in particle size but the number concentration was conserved. The

436   number mean diameter and the number concentration data - representing the initial condensational sink –

437   for all experiments are listed in Table 1.

438

439   New particle formation and growth was observed for most experiments at or near the highest

440   photochemical ages (at or >1 OH day), which presumably influenced the condensational sink at the

441   beginning of the experiment. Therefore, we performed sensitivity simulations to investigate the influence

442   of new particle formation on model predictions. We performed simulations with each model (VBS and

443   SOM) with four different initial condensational sinks. The first three simulations used measured data to

444   calculate the initial condensational sink inputs: (i) number mean diameter and measured number

445   concentration at no OH exposure (equivalent to the default for non-DPF+DOC experiments), (ii) number

446   mean diameter and measured number concentration at the given OH exposure, and (iii) average of (i) and

447   (ii) (default for DPF+DOC experiments). The fourth simulation (iv) assumed that the OFR nucleated 1

448   nm particles at the beginning of the experiment where the number concentration of these particles was

449   equal to that measured at the end of the experiment.

450

2.5 Model Simulations and Model Code

452   The VBS and SOM models were run separately for each photochemical exposure simulated for each

453   experiment listed in Table 1. In the VBS simulations, POA was tracked in one basis set while products

14

454   from each SOA precursor were tracked in separate basis sets, allowing us to distinguish between POA and

455   SOA. In the SOM simulations, all precursor molecules with the same surrogate (e.g., all *n*-alkanes) were

456   tracked in the same SOM grid. Model simulations were performed in phases to answer specific questions

457   and inform model inputs for later simulations:

458   1. To provide a general overview of the model predictions and model-measurement comparison, and

459   to orient the reader to the results thereafter, we performed simulations with the VBS and SOM

460   models using the base set of inputs for one of the Idle-Diesel-None experiments. Our base case

461   included: Profile #3161 for VOC emissions, 30% IVOC mass fraction, kinetic gas/particle

462   partitioning with a mass accommodation coefficient of 0.1, and monodisperse aerosol inputs based

463   on measured data at no photochemical exposure. The partitioning- and IVOC-related choices for

464   the base case are discussed in Sections 3.2 and 3.3 respectively.

465   2. Models used to simulate SOA production in environmental chambers and OFRs have typically

466   assumed instantaneous equilibrium partitioning (e.g., Chen et al. (2013)). To examine the validity

467   of assuming instantaneous equilibrium partitioning, we performed simulations with the VBS and

468   SOM models using instantaneous or kinetic gas/particle partitioning for one of the Idle-Diesel-

469   None and the Idle-Diesel-DPF+DOC experiments. Kinetic partitioning was modeled using three

470   values of the mass accommodation coefficient (α=0.01, 0.1, 1) to capture the uncertainty in its true

471   value. To examine the influence of an increased initial condensational sink from new particle

472   formation on kinetic partitioning, we performed additional simulations using four different initial

473   condensational sinks (see Section 2.4.3) on one of the Idle-Diesel-None and the Idle-Diesel-

474   DPF+DOC experiments.

475   3. Previous work has shown that combustion-related IVOCs are important precursors of SOA (e.g.,

476   Jathar et al. (2014b)). To investigate the importance of IVOCs, we performed simulations with the

477   VBS and SOM models at four different assumed IVOC mass fractions (0%, 13.76%, 30%, and

478   60%), as discussed above when discussing the THC profiles, at all photochemical exposures and

479   for all the experiments listed in Table 1. We performed additional simulations with different

480   emissions profiles and SOA parameterizations on one of the Idle-Diesel-None experiments to

481   investigate uncertainties linked to the composition and SOA potential of IVOCs.

482   4. Additional simulations were performed to examine the sensitivity of model predictions to the

483   following processes: multi-generational aging, vapor wall losses, residence time distributions, and

484   spatial heterogeneity in OH concentrations.

485   The numerical codes for the VBS were developed in Matlab while those for the SOM were developed in

486   IGOR (WaveMetrics Inc.). These codes will be made available on request. The simulations were

487 performed on an Intel i5 processor (1.7 GHz) and required ~10 s to perform a VBS simulation and ~500 s

488 to perform a SOM simulation at a single photochemical exposure.

489

490 **3. Results**

491 **3.1 General Model Results Using the Base Case**

492 In Figure 1, we compare predictions of OA from the VBS and SOM models using the base case to the

493 measurements for the Idle-Diesel-None experiment performed on June 5. Figures 1(a) and 1(b) compare

494 predictions to the measurements in units of µg m^{-3} and g kg-fuel^{-1}, respectively; hereafter we present all

495 mass predictions in units of g kg-fuel^{-1}. For this experiment, the VBS/SOM models over-predicted the OA

496 mass by a factor of 1.9/2.2 at the lowest photochemical exposure (0.06 OH days) and a factor of 1.6/1.8 at

497 the next highest photochemical exposure (0.17 OH days). The over-prediction was because the models

498 significantly over-predicted the SOA formation at these two photochemical exposures. For higher

499 photochemical exposures (>0.5 OH days), both models slightly under-predicted the OA mass but

500 predictions were still within the measurement uncertainty. Our base case seemed to offer a mixed model-

501 measurement comparison for this specific experiment (i.e., over-prediction at lower photochemical ages

502 and a slight under-prediction at higher photochemical ages) because the 30% IVOC mass fraction used in

503 the base case was optimized to achieve a favorable model-measurement comparison across all

504 experiments at all photochemical exposures. In other words, the over-prediction in this experiment at

505 lower photochemical exposures was probably offset by an under-prediction at similar photochemical

506 exposures for some of the other experiments. It is important to note that the model performance varied

507 across the suite of experiments and this overall model performance is discussed in more detail in Section

508 3.3. The VBS and SOM models predicted that the OA at the maximum photochemical exposure was

509 dominated by SOA produced from VOC and IVOC oxidation (92-93%), which agreed well with the

510 measured composition (see Figure 1(c)). For the measurements, POA was defined as fresh OA while SOA

511 was defined as OA formed in addition to the POA. Furthermore, both models suggested that most of the

512 SOA emanated from the oxidation of IVOCs with only 7-14% resulting from the oxidation of aromatic

513 VOCs and less than 0.6-4% resulting from alkane VOCs smaller than a C_{12}. This dominance of IVOCs in

514 explaining the photochemically produced SOA is in line with previous OFR and chamber studies that

515 have modeled SOA formation from diesel exhaust (Tkacik et al., 2014;Zhao et al., 2015;Jathar et al.,

516 2014b).

517

518 **3.2 Kinetic Gas/Particle Partitioning**

519 In Figure 2, we plot predictions from the VBS and SOM models for the Idle-Diesel-None and Idle-Diesel-

520 DPF+DOC experiments assuming instantaneous and kinetic gas/particle partitioning. The two different

521 experiments were deliberately chosen to highlight the role instantaneous partitioning plays at the

522 extremities. We found that for the Idle-Diesel-None experiment, the use of instantaneous partitioning

523 roughly produced the same result as kinetic partitioning with α values of 0.1 and 1 and that all these

524 predictions resulted in roughly the same model-measurement comparison. The instantaneous partitioning

525 predictions were slightly higher than the kinetic partitioning predictions for the VBS simulations. The

526 kinetic partitioning simulations (except for that with an α of 0.01) produced the same result as the

527 instantaneous partitioning simulation most likely because the initial condensational sink was large enough

528 (1.12 min^{-1}) in this experiment that there were no kinetic limitations to partitioning. The increase in the

529 condensational sink through condensation of SOA (10 min^{-1} at the highest photochemical exposure)

530 tended to further reduce any differences in the predictions between the kinetic and instantaneous

531 partitioning simulations. However, for the Idle-Diesel-DPF+DOC experiment, the instantaneous

532 partitioning simulation predicted substantial OA mass at the lower photochemical exposures (0.04 and

533 0.12 OH days) compared to the kinetic partitioning simulations, specifically a factor of 9.8-29 larger at

534 0.04 OH days and a factor of 9.7-75 larger at 0.12 OH days for the VBS model and a factor of 3.9-5.8

535 larger at 0.04 OH days and a factor of 6.4-9.1 larger for the SOM. The instantaneous partitioning

536 simulations predicted a lot more SOA because all condensable products of organic precursor oxidation

537 were allowed to condense instantaneously (according to their respective volatilities) while the kinetic

538 partitioning simulations predicted little SOA production because the initial condensational sink was quite

539 small (0.002 min^{-1}). Predictions from the instantaneous and kinetic partitioning simulations were much

540 closer at the higher photochemical exposures because the SOA formed had grown the condensational sink

541 enough to reduce limitations to partitioning (1 min^{-1} at the highest photochemical exposure). These results

542 imply that the condensation of SOA in OFRs, in some instances, could be kinetically-limited and that

543 instantaneous partitioning may result in models over-predicting the condensation and formation of SOA.

544

545 We make two additional observations based on the results in Figure 2. First, the initial condensational

546 sink for the Idle-Diesel-None experiment was large (1.12 min^{-1}) compared to condensational sinks one

547 would encounter in the real atmosphere. For example, 5 μg m^{-3} of aerosol in a representative rural or

548 remote environment will have a condensational sink <0.05 min^{-1} (Seinfeld and Pandis, 2006). Therefore,

549 modeling ambient applications of the OFR or OFR use with sources that use emissions control devices

550 will need to be even more mindful of the instantaneous partitioning assumption while predicting SOA

551 formation. Second, for the kinetic partitioning results, predictions from both models were relatively less

552 sensitive to α values between 0.1 and 1 but were dramatically lower for an α value of 0.01; more than a

553   factor of 2 for the Idle-Diesel-None experiment and more than an order of magnitude for the Idle-Diesel-

554   DPF+DOC experiment. Given the low sensitivity to α values greater than 0.1 and the reasonable model-

555   measurement comparison at an α value of 0.1 and 1 at least for the Idle-Diesel-None experiment, we

556   argue that the SOA condensation can be represented by an α value larger than 0.1 for the OFR

557   experiments in this work. This α value for diesel exhaust SOA was consistent with prior estimates of the α

558   value for biogenic SOA estimated from chamber, OFR, and aerosol heating experiments (Lee et al.,

559   2011;Saleh et al., 2013;Karnezi et al., 2014;Palm et al., 2016) and direct measurements of α for alkanol

560   SOA (Krechmer et al., 2017). However, an α of 0.1 was an order of magnitude higher than that observed

561   recently for toluene SOA under dry conditions (Zhang et al., 2014). Model results presented hereafter

562   include a kinetic treatment of gas/particle partitioning and assumed an accommodation coefficient of 0.1.

563

564   Results from model simulations performed using different initial condensational sink inputs, some of

565   which captured the influence of new particle formation, are plotted in Figure 3. We found that the initial

566   condensational sink had no influence on the OA predictions from both models for the Idle-Diesel-None

567   experiment, despite substantial differences in the initial condensational sink between the different cases.

568   This was because the amount of SOA formed (920 μg m^{-3} at the highest photochemical exposure) was

569   sufficient to grow the condensational sink enough that the initial condensational sink did not matter. In

570   contrast, for both models we found large differences between the model predictions of OA for the Idle-

571   Diesel-DPF+DOC experiment. The use of inputs based on the measurements at no OH exposure, where

572   the aftertreatment system significantly reduced number concentrations (910 cm^{-3}) and hence the available

573   condensational sink (0.002 min^{-1}), produced much less SOA (an order of magnitude lower or more) and

574   poorer agreement with the measurements (see curve (i) in Figure 3(b)). Initial condensational sinks that

575   captured the influence of new particle formation resulted in higher model predictions but were still about

576   a factor of ~2 lower for the VBS simulations and a factor of ~2.7 lower for the SOM simulations when

577   compared against the measurements. The DPF+DOC results also suggest that calculating an initial

578   condensational sink using data from before and after the photochemical exposure, as done by Palm et al.

579   (2016), could be used as an input to model OFR data. Slight differences between the different curves for

580   the Idle-Diesel-None experiment and curves (ii), (iii), and (iv) for the Idle-Diesel-DPF+DOC experiment

581   can be attributed to the interaction of multigenerational aging and kinetic gas/particle partitioning.

582

583   **3.3 Influence of IVOCs on SOA Formation**

584   In Figure 4(a), we compare predictions of SOA concentrations from the SOM against measurements for

585   all the experiments listed in Table 1 and at all photochemical exposures. For visual clarity, we do not

586   present results from the VBS model as both models had nearly identical predictions with a few

587   exceptions; see Figure S1 where we compare VBS model predictions to SOM predictions for all

588   experiments at all photochemical exposures for the base case. The four panels in Figure 4(a) show model-

589   measurement comparisons assuming four different fractions of IVOCs: 0%, 13.76%, 30%, and 60%;

590   statistical metrics of fractional bias, fractional error, and R^2 for the comparison for both models are listed

591   in Table S4 (fractional bias $= \frac{1}{N}\sum_{i=1}^{n}\frac{M-O}{\frac{M+O}{2}}$, fractional error $= \frac{1}{N}\sum_{i=1}^{n}\frac{|M-O|}{\frac{M+O}{2}}$, M=predicted value,

592   O=observed value, N=sample size). The model-measurement comparison and the model skill was very

593   poor when no IVOCs were included (fractional bias = -109%, fractional error = 125%, and R^2 = 0.52);

594   this model reflects the treatment of diesel-powered sources in most traditional emissions inventories and

595   large-scale models. The model-measurement comparison was reasonable with 13.76% IVOCs (fractional

596   bias = -46%, fractional error = 101%, and R^2 = 0.95) but model predictions were over-predicted with 60%

597   IVOCs (fractional bias = 72%, fractional error = 97%, and R^2 = 0.99). The optimal model performance

598   that produced the lowest fractional bias and fractional error was realized at an IVOC mass fraction of 30%

599   (fractional bias= 6%, fractional error= 86%, and R^2 = 0.88). For predictions with an IVOC mass fraction

600   of 30%, 66% and 70% of the model predictions were within a factor of 1.5 and 2 of the measurements and

601   IVOCs on average accounted for 67%/72% (VBS/SOM) of the SOA at the highest photochemical

602   exposure across all experiments. Given the optimal performance, the base case used in this work assumed

603   a 30% IVOC fraction. These comparisons indicate that it is critical that IVOCs be included when

604   modeling the SOA formation from diesel exhaust and also validate the IVOC composition estimates made

605   by Zhao et al. (2015). We note that the model of Peng and Jimenez (2017) suggested that the organic

606   compounds in the OFR experiments performed by Jathar et al. (2017) may have been subjected to non-

607   tropospheric photolysis at 185 and 254 nm. Accounting for the photolysis of the key SOA precursors

608   (IVOCs and aromatics) could affect the optimal IVOC fraction identified above and hence needs to be

609   considered in future work.

610

611   We further investigated the IVOC species that contributed the most to SOA formation. For an IVOC

612   fraction of 30%, cyclic alkane IVOCs accounted for 23% of the THC emissions and on average accounted

613   for 61%/53% (VBS/SOM) of the SOA formation across the different experiments. We should note that

614   the speciation of cyclic alkane IVOCs in Zhao et al. (2015), while robust in quantifying the carbon

615   number, did not include any specificity in terms of the molecular structure, i.e., their methods would not

616   be able to distinguish between a pure C_{10} cyclic alkane and a cyclohexane with a 4-carbon branch.

617   Further, the parameterizations to model SOA formation from cyclic alkane IVOCs for both models were

618   based on the behavior of particular compounds. In the VBS model when using the high NO_X
619   parameterizations, the surrogate for a cyclic alkane IVOC was determined through equivalence with a
620   straight alkane IVOC while in the VBS model when using the low NO_X parameterizations or the SOM the
621   cyclic alkane IVOCs were tied to parameterizations for hexylcyclohexane. (The observed SOA yield and
622   derived SOM parameterization for hexylcyclohexane is actually quite similar to that for cyclododecane
623   for low-NO_X conditions, but not for high-NO_X conditions (Cappa et al., 2013)) This lack of specificity in
624   the speciation and the SOA parameterizations made the SOA predictions from the oxidation of cyclic
625   alkane IVOCs relatively uncertain. To examine the sensitivity of the model predictions to uncertainties in
626   the model treatment of cyclic alkane IVOCs, we performed simulations with both models for one of the
627   Idle-Diesel-None experiments where the cyclic alkane IVOCs were treated as branched alkane IVOCs;
628   results from these simulations are shown in Figure 5(a). The use of branched alkane IVOCs to model
629   cyclic alkane IVOCs only marginally reduced OA predictions for both the VBS and SOM models,
630   suggesting that the model predictions were not sensitive to the SOA parameterization used for cyclic
631   alkane IVOCs. Regardless, we recommend that future work focus on a more detailed speciation of cyclic
632   alkane IVOCs in combustion emissions as well as on chamber and OFR experiments on those speciated
633   compounds to improve quantification of their SOA mass yields.

634

635   As there were no direct measurements of any SOA precursors in the study of Jathar et al. (2017a), we
636   have used previously published emissions profiles for diesel exhaust to determine initial concentrations of
637   the SOA precursors. We examined the sensitivity of model predictions to two different emissions profiles
638   from the EPA SPECIATE (version 4.3) database: Profile #3161 (included in the base case) and Profile
639   #8774 that represents emissions from 'Heavy Duty Diesel Exhaust'; the speciation for both profiles is
640   provided in Tables S2 and S3. Both profiles only included speciation for VOC emissions and in these
641   simulations we assumed an IVOC mass fraction of 30%. The results captured in Figure 5(b) for one of the
642   Idle-Diesel-None experiments show that the choice in the emissions profile had no influence on the OA
643   evolution for the VBS model but had a small influence on the OA evolution for the SOM. This little to
644   small influence was expected given that most of the SOA was formed from IVOC, rather than VOC,
645   oxidation. This further demonstrates that IVOCs, not VOCs, play an important role in controlling the
646   SOA formation from diesel exhaust emissions and it is important that future studies work towards better
647   understanding the IVOC speciation.

648

649   The IVOC speciation of Zhao et al. (2015) included 37 unique species, each of which required a unique
650   surrogate to model the SOA formation from that species. Tracking these many IVOC species in an

651 atmospheric model (e.g., global climate model) may be intractable and hence, there is a need to develop

652 simplified parameterizations to efficiently model SOA formation from IVOCs. We note that species using

653 the same surrogate in the VBS model (e.g., a C_{15} linear alkane, C_{17} branched alkane, and C_{13} cyclic alkane

654 are all parameterized using *n*-pentadecane when using the high NO_X parameterizations) could be lumped

655 together to reduce the number of precursors and products tracked and that there are no penalties for a

656 precursor type (e.g., *n*-alkanes) to include additional precursor and product species once a SOM grid is

657 setup. Nonetheless, to investigate the possibility of developing a simplified parameterization, we modeled

658 SOA from IVOCs assuming that all the IVOCs could be modeled together as a single linear C_{13}, C_{15}, C_{17}

659 or C_{19} alkane; a similar strategy was employed by (Jathar et al., 2014b) to model SOA formation from

660 unspeciated organic compounds in combustion emissions. Results from these simulations are shown in

661 Figure 5(c) for one of the Idle-Diesel-None experiments. For the VBS model, the use of a larger carbon

662 number alkane to model IVOC SOA produced increasingly more OA, with the C_{19} alkane providing the

663 best comparison against measurements. For the SOM, the use of a C_{13} and C_{15} alkane produced good

664 agreement with measurements with a C_{13} alkane slightly under-predicting the OA at 0.5 OH days and the

665 C_{15} alkane slightly over-predicting the OA at lower photochemical exposures (0.06 and 0.17 OH days). It

666 was interesting to observe that for the SOM, in contrast to the VBS, the use of different linear alkanes

667 produced different OA masses at lower photochemical exposures but converged at the highest

668 photochemical exposure suggesting that the effective SOA mass yield in the SOM varied dynamically

669 with photochemical age. Differences in the VBS and SOM predictions with different alkane

670 parameterizations point to inherent differences in the coupled representation of multigenerational aging

671 and gas/particle partitioning. Results from these simulations indicate that in cases where computational

672 efficiency is demanded, the SOA formation from IVOCs in diesel exhaust could be modeled using a

673 surrogate linear alkane, possibly a C_{19} linear alkane with the VBS and a C_{13} or C_{15} linear alkane for the

674 SOM.

675

676 3.4 Elemental Composition

677 The SOM tracks both the carbon and oxygen number of the oxidation products, which allowed us to

678 predict the O:C ratio of the OA. The O:C of the OA was calculated by combining the measured O:C of

679 the POA with the modeled O:C of the SOA. We compare predictions of the O:C of OA from the SOM

680 against measurements for all the experiments listed in Table 1 and at all photochemical exposures in

681 Figure 4; statistical metrics of fractional bias, fractional error, and R^2 for the comparison are listed in

682 Table S5. Model predictions for the no IVOC case, where the O:C of the OA was dominated by the O:C

683 of the aromatic SOA, compared well with measurements (fractional bias = -4.2%, fractional error = 28%,

684   and $R^2 = 0.77$). However, the poor OA mass predictions with no IVOCs suggests that the good O:C

685   performance was purely coincidental. The 13.76%, 30%, and 60% IVOC cases under-predicted the OA

686   O:C where the under-prediction appeared to increase as the IVOC influence increased; fractional bias = -

687   32%, fractional error = 38%, and $R^2 = 0.72$ for the 13.76% IVOC case, fractional bias = --37%, fractional

688   error = 42%, and $R^2 = 0.70$ for the 30% IVOC case, and fractional bias = -60%, fractional error = -62%,

689   and $R^2 = 0.46$ for the 60% IVOC case. A higher IVOC fraction resulted in a lower O:C ratio because the

690   IVOCs were primarily composed of higher carbon number species that on oxidation produced low O:C

691   SOA compared to SOA formed from precursors such as aromatics. On average, the 30% IVOC case

692   predicted an O:C ratio that was 28% lower than the measurements. For the three non-zero IVOC cases

693   (13.76%, 30%, and 60%), the model skill in predicting the O:C was much better for the non-DPF+DOC

694   experiments ($R^2 = 0.82$, 0.83, and 0.80 respectively) than for the DPF+DOC experiments ($R^2 = 0.02$, 0.02,

695   and 0.29 respectively). Measurements and model predictions of the OA O:C ratio from the 30% IVOC

696   case as a function of photochemical age are presented in Figure S2.

697

698   The under-prediction in O:C ratios was confounding when compared to earlier applications of the SOM

699   and in light of the reasonable model-measurement comparison found in this work in predicting OA mass.

700   We note that the low O:C in the 13.76%, 30%, and 60% IVOC cases stems from the dominance of

701   product species that have high carbon numbers and low oxygen numbers. We explored several lines of

702   reasoning for this under-prediction. First, Cappa et al. (2013) found good agreement between the SOM-

703   predicted and observed O:C for chamber experiments conducted using individual linear, branched and

704   cyclic C_{12} alkanes. Also, general predictions of the dependence of O:C on the carbon number of the parent

705   hydrocarbon (cf. Fig. 2b in Cappa and Wilson (2012)) show good agreement with observations (cf. Fig.

706   2a in Tkacik et al. (2012)), both in terms of absolute values and shape. This suggests that uncertainties in

707   the SOM parameters may not be the dominant reason for the under-prediction. A possible reason for the

708   under-prediction then is that the compounds identified by Zhao et al. (2015) as IVOCs are structurally

709   different than the alkanes used to model them in this work. Second, the gas-phase chemistry in the OFR

710   might be inherently different than that in a chamber. For example, kinetic limitations to gas/particle

711   partitioning may result in gas-phase oxidation of low-volatility products having high O:C that typically

712   would have partitioned to the particle phase in a chamber experiment but instead are fragmented (Palm et

713   al., 2016). As to why the chamber-based SOM parameters then offer good model performance on OA

714   mass remains unclear. One way in which this issue could be addressed in the future is by developing

715   SOM parameters exclusively based on OFR data, as and when they become available. Third, the SOM

716   used here did not include surface/heterogeneous and particle-phase reactions that might influence the OA

composition and O:C ratio. When heterogeneous reactions of OA were included assuming an OH uptake coefficient of 1 (the product distribution from the oxidation reaction was kept the same as the gas-phase reactions), SOA production at the highest photochemical exposure for all the experiments was reduced, on average, by 7% from fragmentation reactions within the particle phase, but the O:C ratio was only marginally increased (average of 2%).

To understand the O:C under-prediction better, we compared model predictions of normalized gas-phase species concentrations from the SOM to normalized gas-phase measurements made by Friedman et al. (2017) using a chemical ionization mass spectrometer (CIMS). The CIMS detects an array of oxygenated organic species and the high resolution of the time-of-flight mass spectrometer enables identification of the elemental composition of each detected peak. The CIMS data were aggregated by carbon and oxygen number to facilitate comparison with the SOM data. The comparison was performed on a normalized basis because the CIMS did not provide absolute concentrations for every detected peak. The SOM-CIMS comparisons for the Idle-Diesel-None and Load-Diesel-None experiments at the highest photochemical exposure are shown in Figure 6, which highlight four findings of note. First, the CIMS measured species larger than a carbon number of 12 that are presumably products from oxidation of higher molecular weight organic compounds, although the possibility of dimer formation in the instrument cannot be entirely ruled out. Nonetheless, this provides additional evidence for the presence of IVOC oxidation products in diesel exhaust emissions. Second, the CIMS measured organic compounds with high O:C ratios (e.g., C_6O_6, C_7O_7). This implies that the reaction chemistry in OFRs rapidly adds functional groups to the carbon backbone, although larger, less oxidized compounds could be simultaneously functionalized and fragmented in the CIMS leading to the appearance of highly oxidized species. Third, the SOM offered a reasonable correlation against the CIMS measurements for both experiments across a majority of the carbon-oxygen combinations that spanned more than four orders of magnitude. Qualitatively, this finding validates the statistical evolution of organic compounds tracked through the generalized SOM mechanism, although certainly some differences are evident. Finally, for the mid-carbon number species ($\sim C_{10}$), the SOM seemed to produce higher fractions of species with low oxygen numbers (O_0 to O_3) but lower fractions of species with high oxygen numbers (O_5 to O_7). This under-prediction of the high oxygen number species might potentially explain why the SOM may be under-predicting the OA O:C ratio. The SOM-CIMS comparison is preliminary and we intend to explore the implications of this comparison in future work.

3.5 Other Model Sensitivities

750   We performed sensitivity analyses to examine the influence of other key processes on predictions from

751   both the VBS and SOM models. When examining the sensitivity to each process, all the other inputs were

752   kept the same as those listed in the base case. We only present sensitivity results for the Idle-Diesel-None

753   experiment performed on June 5, as the results for this experiment were generally representative of all

754   experiments (Figure 7). For completeness, we performed simulations for all the experiments at the highest

755   photochemical exposure since each of the processes explored below manifested the strongest response at

756   the highest photochemical exposure. The results from these simulations are presented as a change in the

757   model predictions relative to that offered by the base case.

758

759   ***Multi-generational Aging.*** One of the key differences between the VBS and the SOM models is how they

760   represent the multi-generational aging of gas-phase products. SOA parameters for the VBS model

761   represent stable product distributions at the end of the chamber experiments and therefore already include

762   the influence of multi-generational aging reactions encountered during the chamber experiment.

763   Additional multi-generational aging in the VBS model, based on the scheme of Robinson et al. (2007), is

764   simulated as a continuous decrease in product volatility, which does not account for fragmentation

765   reactions and has not been constrained against experiments. The SOM framework explicitly models multi-

766   generational aging that includes treatment of fragmentation reactions and constrains the aging reactions

767   based on the chamber experiments to an extent that is determined by the length (in OH exposure space) of

768   the experiment. To test the influence of multi-generational aging, we performed model simulations with

769   aging turned off for the VBS and SOM models and plot the results in Figure 7(a). We found that aging

770   had a small influence (~18% reduction in OA mass) on model predictions from the VBS model, most

771   likely because the high SOA and OA mass concentrations resulted in a substantial fraction of the organic

772   species to be partitioned to the particle phase. This left very little of the organic species in the gas-phase to

773   participate in multi-generational aging. We calculated that less than 20% by mass of the product species

774   in this experiment was in the gas-phase at the OA mass concentration at the highest photochemical

775   exposure, implying that the SOA mass yields at these OA mass concentrations were rapidly approaching

776   100%. In contrast, the absence of aging resulted in a 43% decrease in the OA mass for the SOM. The

777   decrease was mainly because the first generation oxidation product with the highest yield (i.e., C_xO_1) was

778   too volatile to partition to the particle phase and needed to be aged further to form condensable products.

779   As noted earlier, the term aging is defined differently for the VBS and SOM models and the results

780   presented here need to take the definitional issues into account when examining the influence of aging.

781   Compared to the base case, no aging resulted in an average decrease of 4% and 30% in OA mass for the

782   VBS and SOM models respectively for all experiments at the highest photochemical exposure. These

783   simulations suggest that aging of the oxidation products, at least for the SOM, is as important as the

784   contribution of first generation products to SOA formation.

785

786   ***Vapor Wall Losses.*** Prior work has highlighted the influence vapor wall losses exert on the calculation of

787   SOA mass yields from chamber experiments (Zhang et al., 2014;Krechmer et al., 2016). Cappa et al.

788   (2016), based on the chamber work of Zhang et al. (2014), recently published parameter sets for the SOM

789   that accounted for no vapor wall losses and two different vapor wall loss rates (1×10^{-4} and 2.5×10^{-4} s^{-1})

790   assuming an equivalent OA mass of the chamber walls of 10 mg m^{-3} (the base case used the parameter

791   sets for a vapor wall loss rate of 2.5×10^{-4} s^{-1}). We performed model simulations with SOM using

792   parameters that were either not corrected for vapor wall losses or that were corrected for vapor wall losses

793   using either the low (1×10^{-4}) or high (2.5×10^{-4}) estimates proposed by Cappa et al. (2016). The results

794   plotted in Figure 7(b) show that correcting for vapor wall losses significantly increased model predicted

795   OA mass (by 73% and 112% for the low wall loss and high wall loss cases respectively at the highest

796   photochemical exposure when compared to the no wall loss case) and provided the best performance for

797   the high estimate for vapor wall losses. Across all experiments and at the highest photochemical exposure,

798   accounting for vapor wall losses using the high estimate resulted in an average increase of 39% over no

799   accounting for vapor wall losses. These comparisons suggest that it is important to use SOA

800   parameterizations in which vapor wall losses in chambers have been accounted for when interpreting

801   SOA experiments. Furthermore, we also simulated the influence of vapor losses to the OFR walls on

802   model predictions. We assumed reversible uptake of vapors to the walls and used a vapor wall loss rate of

803   2.5×10^{-3} s^{-1} (factor of ~10 larger than that for a chamber) based on the work of Palm et al. (2016) and an

804   equivalent OA mass concentration of 10 mg m^{-3} for the OFR walls. The results plotted in Figure 7(b)

805   show that the loss of vapors to the OFR walls had a small influence on model predictions: a 6.5%

806   decrease for this experiment and an average decrease of 11% across all experiments at the highest

807   photochemical exposure. Increasing the equivalent OA mass concentration for the OFR walls to 100 and

808   1000 mg m^{-3} seemed to have no influence on model predictions. These findings imply that vapor wall

809   losses in the presence of sufficient seed aerosol might not be of concern for OFRs (Lambe et al., 2015).

810

811   ***Residence Time Distributions.*** Model simulations performed in this work assumed that the OFR operated

812   as a plug flow reactor with a constant residence time. Experimental studies by Lambe et al. (2011) and

813   fluid dynamics simulations by Ortega et al. (2016) have shown that OFRs, particularly like the one used

814   in this work, exhibit heterogeneity in residence times. We performed simulations to explore the sensitivity

815   of varying residence times on model predictions. These simulations were performed based on a

816 discretized version of the residence time distribution measured by Lambe et al. (2011) for SO_2 that

817 yielded an average residence time of 100 seconds (same as that used by Jathar et al. (2017a)). The

818 discretized version included six parcels with volume fractions of 0.23, 0.36, 0.24, 0.11, 0.05, and 0.01

819 with residence times of 45, 65, 100, 200, 300, and 500 seconds respectively. Each parcel experienced the

820 same OH concentration but the varying residence times resulted in different OH exposures for each

821 parcel. The parcels were combined after photochemical exposure without repartitioning the OA between

822 the six parcels. Similar to the findings of Peng et al. (2015) for calculating OH exposure, our results in

823 Figure 7(c) show that using a residence time distribution had very little influence on the OA mass

824 evolution compared to use of an effective average time. Compared to the base case, the residence time

825 distribution resulted in an average decrease of 3% and 5% in OA mass for the VBS and SOM models

826 respectively for all experiments at the highest photochemical exposure.

827

828 ***Spatial Heterogeneity in OH.*** In addition to the influence exerted by a distribution of residence times,

829 spatial heterogeneity in the gas-phase chemistry inside the OFR (e.g., from radial variation in light

830 intensity) could lead to spatial heterogeneity in OH concentrations and result in a distribution of OH

831 exposures for the sample being aged. We performed simulations to explore the sensitivity of a varying

832 OH exposure on model predictions. These simulations were performed where we split the sample coming

833 into the OFR into two parcels and treated the parcels to different OH exposures. Each experiment was

834 repeated for all combinations (six total) of three different parcel splits (¼-¾, ⅓-⅔, ½-½) and two different

835 OH exposure splits (⅓-X, ⅔-X); X was determined by conserving the total OH exposure reported by

836 Jathar et al. (2017a). For instance, the first simulation was performed by splitting the OFR air parcel into

837 ¼ and ¾ fractions by volume and exposing the ¼ volume to ⅓ the OH exposure. The parcels were

838 combined after photochemical exposure without repartitioning the OA between the two parcels. The

839 results in Figure 7(d) show that the simulated spatial heterogeneity always reduced the OA mass although

840 the maximum reduction (13% for the VBS and 14% for the SOM models) at the highest photochemical

841 exposure was within the measurement uncertainty at least for the SOM. Compared to the base case, the

842 spatial heterogeneity in OH resulted in a maximum decrease of 13% and 15% in OA mass for the VBS

843 and SOM models respectively for all experiments at the highest photochemical exposure.

844

845 **4. Summary and Discussion**

846 Recently, Jathar et al. (2017a) reported on experiments performed using the oxidation flow reactor (OFR)

847 to measure the photochemical production of secondary organic aerosol (SOA) from diesel exhaust under

848 varying engine loads, fuel types, and aftertreatment systems. These data present an opportunity to not only

849   test SOA models but also use these models to interpret OFR data and determine their relevance for the

850   real atmosphere. In this work, we applied two different SOA model frameworks (VBS and SOM) to

851   simulate the photochemical production of SOA in an OFR from diesel exhaust and evaluated those model

852   frameworks using the data from Jathar et al. (2017a). The volatility basis set (VBS) model is a

853   parameterized model that allows for a volatility-based representation of OA while the statistical oxidation

854   model (SOM) is a semi-explicit parameterized model that uses a carbon-oxygen grid to track OA. Both

855   simulated the coupled chemistry, thermodynamic properties, and gas/particle partitioning of OA and

856   accounted for: (i) semi-volatile and reactive emissions of primary organic aerosol (POA), (ii) SOA

857   production from IVOCs and VOCs, (iii) multi-generational aging, and (iv) kinetic gas/particle

858   partitioning.

859

860   Model predictions suggest that the instantaneous gas/particle partitioning assumption may over-predict

861   SOA formation in OFRs when the initial condensational sinks are low and the condensation of SOA is

862   likely kinetically limited. Hence, SOA formation in OFRs needs to be modeled/interpreted through an

863   explicit treatment of kinetic gas/particle partitioning. Differences in model predictions between

864   instantaneous and kinetic partitioning will depend on the rate at which condensable SOA mass is

865   produced in the OFR (depends on the initial precursor concentrations and photochemical exposure),

866   residence time in the OFR, properties of the condensing species (e.g., diffusion coefficient, molecular

867   weight), and parameters relevant for partitioning (e.g., accommodation coefficient, seed aerosol surface

868   area). To explore the relative importance of instantaneous and kinetically-limited partitioning in an OFR,

869   we used the SOM to simulate SOA formation from diluted diesel exhaust using instantaneous and kinetic

870   partitioning assumptions for varying amounts of SOA formed (1-10000 $\mu g\ m^{-3}$) and initial condensational

871   sinks (0.001-10 min^{-1}). These simulations were similar to the calculations performed by Palm et al. (2017)

872   where they calculated timescales and losses of condensable SOA vapors to the OFR walls and sampling

873   lines and reaction with OH. The calculations were performed for two different initial particle sizes (10

874   and 100 nm) since the condensation of SOA mass would grow the initial condensational sink for the two

875   particles at different rates, i.e. for the same starting initial condensational sink, smaller particles would

876   experience quicker growth in the condensational sink compared to larger particles for the same amount of

877   condensing mass. The calculations were also performed for two different residence times – 2 and 4

878   minutes – to span the residence time range used in typical applications of the OFR. We assumed an

879   accommodation coefficient of 0.1. The results plotted in Figure 8 show the ratio of SOA predicted

880   through kinetic partitioning to that predicted through instantaneous partitioning as a function of the initial

881   condensational sink and the SOA formed under an instantaneous partitioning assumption. Across the four

882   scenarios explored (two initial particle sizes and two residence times), the SOA formation predicted under

883   the kinetic partitioning assumption was an order of magnitude or more lower than that predicted under the

884   instantaneous partitioning assumption over a large portion of the input range explored, e.g., when the

885   initial condensational sink was smaller than ~0.1 min^{-1} and the maximum SOA formed was lower than

886   ~100 µg m^{-3} for the 10 nm simulations and lower than ~1000 µg m^{-3} for the 100 nm simulations. We also

887   found that the SOA formation in the OFR was kinetically-limited under typical ambient conditions. The

888   SOA formation predicted under the kinetic partitioning assumption approached the SOA formed under the

889   instantaneous partitioning assumption either when the initial condensational sink was very large (>5 min^{-}

890   ^{1}) or when a large amount of condensable SOA was produced in the OFR (>=1000 µg m^{-3} for the 10 nm

891   particles and >>10000 µg m^{-3} for the 100 nm particles). Our finding implies that ambient applications of

892   the OFR, where initial condensational sinks are typically smaller (~0.005-0.5 min^{-1}) and the maximum

893   SOA produced is typically less than 40 µg m^{-3}, will only produce a small fraction (0-30%) of the intended

894   SOA. Furthermore, our simulations suggested that a smaller initial particle size (i.e., 10 nm) for the same

895   initial condensational sink and a longer OFR residence time (i.e., 4 min) may not necessarily help produce

896   the intended SOA under ambient conditions. Although these simulation results need to be verified

897   experimentally, they do suggest that it might be challenging to operate the OFR in conditions where

898   instantaneous or atmospherically-relevant partitioning is applicable, further complicating the coupled

899   atmospheric simulation of chemistry and thermodynamics in OFRs.

900

901   Upon including IVOCs as SOA precursors, both the VBS and SOM models were able to reasonably

902   predict the OA mass evolution reported by Jathar et al. (2017a) across different engine loads, fuel types,

903   and aftertreatment systems. Model predictions suggest that 30% of the unburned hydrocarbon emissions

904   are likely IVOCs and that these IVOCs (regardless of the emissions profiles used to determine non-IVOC

905   emissions) account for most (average of 70%) of the SOA formed from diesel exhaust. These findings are

906   consistent with prior work from chamber experiments (Jathar et al., 2014b) and modeling studies (Zhao et

907   al., 2015). Simulations performed using single surrogates suggest that the complex mixture of IVOCs in

908   diesel exhaust could be well represented using a linear C_{13} or C_{15} alkane for the SOM but might need a

909   larger surrogate such as a C_{19} alkane for the VBS model. The need for a different surrogate species to

910   model IVOC SOA between the SOM and VBS models most likely arises from differences in the coupled

911   treatment of the oxidation chemistry and gas/particle partitioning in the OFR. The use of surrogates offers

912   a computationally-efficient strategy to model SOA formation from IVOCs in large-scale three-

913   dimensional models. The SOM tracks the carbon and oxygen numbers of the oxidation products and

914   hence model predictions were used to calculate atomic O:C ratios for OA, which were then compared to

measurements. While the inclusion of IVOCs allowed for good model-measurement comparisons on OA mass, the SOM under-predicted the O:C ratio of OA on average by 28%, possibly highlighting the limitations in modeling the IVOCs as alkanes and/or extrapolating chamber-based parameterizations to OFR experiments. Model predictions of the gas-phase organic species compared favorably to those measured using a chemical ionization mass spectrometer (CIMS), which qualitatively validates the statistical evolution of organic compounds tracked through the generalized SOM mechanism.

As OFRs are increasingly used to study SOA formation and evolution in laboratory and field environments, there is a need to develop models that can be used to interpret OFR data. This work suggests that multi-generational aging (in case of the VBS model), residence time distributions, and spatial heterogeneity in OH concentrations produced sensitivities that were well within the measurement uncertainty and were not a concern for the model system studied. However, model predictions did appear to be more sensitive to multi-generational aging (in case of the SOM) and influence of vapor wall losses, highlighting that these processes be included in OFR models. While the conclusions from this work may be relevant for other laboratory and ambient studies, their relative importance may vary. There are several instances where the model development was insufficient and will likely be addressed in future work. For example, the model could benefit from the use of a polydisperse size distribution to treat new particle formation and growth and improve predictions of the evolution of the aerosol size distribution. The model of Peng and Jimenez (2017) suggested that the SOA precursors and their oxidation products in the Jathar et al. (2017) experiments might have been subjected to non-tropospheric photolysis. Our work did not consider the photolysis of IVOCs (or other SOA precursors), which if considered, may have implications for the IVOC findings reported here. We recommend that future studies on combustion sources significantly dilute their emissions before oxidizing them in an OFR while simultaneously accounting for photolysis reactions in models that simulate OFR chemistry. Finally, the model needs to be rigorously tested against other laboratory (e.g., Lambe et al. (2012)) and ambient (e.g., Palm et al. (2016)) OFR data.

5 Acknowledgements

6 References

Ahlberg, E., Falk, J., Eriksson, A., Holst, T., Brune, W. H., Kristensson, A., Roldin, P., and Svenningsson, B.: Secondary organic aerosol from VOC mixtures in an oxidation flow reactor, Atmospheric environment, 161, 210-220, 2017.

Ahmadov, R., McKeen, S. A., Robinson, A. L., Bahreini, R., Middlebrook, A. M., de Gouw, J. A., Meagher, J., Hsie, E. Y., Edgerton, E., Shaw, S., and Trainer, M.: A volatility basis set model for summertime secondary organic aerosols over the eastern United States in 2006, Journal Of Geophysical Research-Atmospheres, 117, D06301, 2012.

Anderson, J. O., Thundiyil, J. G., and Stolbach, A.: Clearing the air: a review of the effects of particulate matter air pollution on human health, Journal of Medical Toxicology, 8, 166-175, 2012.

Atkinson, R., and Arey, J.: Atmospheric degradation of volatile organic compounds, Chemical Reviews, 103, 4605-4638, 2003.

Bond, T., Venkataraman, C., and Masera, O.: Global atmospheric impacts of residential fuels, Energy for Sustainable Development, 8, 20-32, 2004.

Cappa, C., and Wilson, K.: Multi-generation gas-phase oxidation, equilibrium partitioning, and the formation and evolution of secondary organic aerosol, Atmospheric Chemistry and Physics, 12, 9505-9528, 2012.

Cappa, C. D., Zhang, X., Loza, C. L., Craven, J. S., Yee, L. D., and Seinfeld, J. H.: Application of the Statistical Oxidation Model (SOM) to Secondary Organic Aerosol formation from photooxidation of C 12 alkanes, Atmospheric Chemistry and Physics, 13, 1591-1606, 2013.

Cappa, C. D., Jathar, S. H., Wexler, A. S., Seinfeld, J., and Kleeman, M. J.: Simulating secondary organic aerosol in a regional air quality model using the statistical oxidation model – Part 2: Assessing the influence of vapor wall losses, Atmospheric Chemistry & Physics, 16, 3041-3059, 2016.

Chacon-Madrid, H., and Donahue, N.: Fragmentation vs. functionalization: chemical aging and organic aerosol formation, Atmos. Chem. Phys, 11, 10553-10563, doi:10.5194/acp-11-10553-2011 2011.

Chan, A. W. H., Kautzman, K. E., Chhabra, P. S., Surratt, J. D., Chan, M. N., Crounse, J. D., Kurten, A., Wennberg, P. O., Flagan, R., and Seinfeld, J. H.: Secondary organic aerosol formation from photooxidation of naphthalene and alkylnaphthalenes: implications for oxidation of intermediate volatility organic compounds (IVOCs), Atmospheric Chemistry and Physics, 9, 3049-3060, 2009.

Chen, S., Brune, W., Lambe, A., Davidovits, P., and Onasch, T.: Modeling organic aerosol from the oxidation of alpha-pinene in a Potential Aerosol Mass (PAM) chamber, Atmospheric Chemistry and Physics, 13, 5017-5031, 2013.

Chirico, R., DeCarlo, P., Heringa, M., Tritscher, T., Richter, R., Prevot, A., Dommen, J., Weingartner, E., and Wehrle, G.: Impact of aftertreatment devices on primary emissions and secondary organic aerosol formation potential from in-use diesel vehicles: results from smog chamber experiments, Atmospheric Chemistry and Physics, 10, 11545-11563, 2010.

Donahue, N., Robinson, A., Stanier, C., and Pandis, S.: Coupled partitioning, dilution, and chemical aging of semivolatile organics, Environ. Sci. Technol, 40, 2635-2643, doi:10.1021/es052297c, 2006a.

Donahue, N., Epstein, S., Pandis, S., and Robinson, A.: A two-dimensional volatility basis set: 1. organic-aerosol mixing thermodynamics, Atmospheric Chemistry and Physics, 11, 3303-3318, 2011.

Donahue, N. M., Robinson, A. L., Stanier, C. O., and Pandis, S. N.: Coupled partitioning, dilution, and chemical aging of semivolatile organics., Environ. Sci. Technol., 40, 2635-2643, 2006b.

Dzepina, K., Volkamer, R., Madronich, S., Tulet, P., Ulbrich, I., Zhang, Q., Cappa, C., Ziemann, P., and Jimenez, J.: Evaluation of recently-proposed secondary organic aerosol models for a case study in Mexico City, Atmospheric Chemistry

986   and Physics, 9, 5681-5709, doi:10.5194/acp-9-5681-2009, 2009.

987   Ensberg, J. J., Hayes, P. L., Jimenez, J. L., Gilman, J. B., Kuster, W. C., de Gouw, J. A., Holloway, J. S., Gordon, T.
988   D., Jathar, S., and Robinson, A. L.: Emission factor ratios, SOA mass yields, and the impact of vehicular emissions on SOA
989   formation, Atmospheric Chemistry and Physics, 14, 2383-2397, 2014.

990   EPA: SPECIATE Version 4.3, in, 2013.

991   EPA: Estimation Programs Interface Suite™. , in, United States Environmental Protection Agency, Washington, DC,
992   USA., 2017.

993   Friedman, B., Brophy, P., Brune, W. H., and Farmer, D. K.: Anthropogenic Sulfur Perturbations on Biogenic
994   Oxidation: SO2 Additions Impact Gas-Phase OH Oxidation Products of α- and β-Pinene, Environ. Sci. Technol., 50, 1269-
995   1279, 10.1021/acs.est.5b05010, 2016.

996   Friedman, B., Link, M. F., Fulgham, S. R., Brophy, P., Galang, A., Brune, W. H., Jathar, S. H., and Farmer, D. K.:
997   Primary and Secondary Sources of Gas-Phase Organic Acids from Diesel Exhaust, Environ. Sci. Technol., 51, 10872-10880,
998   10.1021/acs.est.7b01169, 2017.

999   Fuzzi, S., Baltensperger, U., Carslaw, K., Decesari, S., Denier van der Gon, H., Facchini, M. C., Fowler, D., Koren, I.,
000   Langford, B., Lohmann, U., Nemitz, E., Pandis, S., Riipinen, I., Rudich, Y., Schaap, M., Slowik, J. G., Spracklen, D. V.,
001   Vignati, E., Wild, M., Williams, M., and Gilardoni, S.: Particulate matter, air quality and climate: lessons learned and future
002   needs, Atmos. Chem. Phys., 15, 8217-8299, 10.5194/acp-15-8217-2015, 2015.

003   Gentner, D. R., Jathar, S. H., Gordon, T. D., Bahreini, R., Day, D. A., El Haddad, I., Hayes, P. L., Pieber, S. M., Platt,
004   S. M., and de Gouw, J. A.: A review of urban secondary organic aerosol formation from gasoline and diesel motor vehicle
005   emissions, Environ. Sci. Technol., 2016.

006   Gordon, T. D., Nguyen, N. T., Presto, A. A., Lipsky, E. M., Maldonado, S., Maricq, M., and Robinson, A. L.:
007   Secondary organic aerosol production from diesel vehicle exhaust: impact of aftertreatment, fuel chemistry and driving cycle,
008   Atmospheric Chemistry & Physics, 14, 4643-4659, doi:10.5194/acp-14-4643-2014, 2014.

009   Hayes, P., Carlton, A., Baker, K., Ahmadov, R., Washenfelder, R., Alvarez, S., Rappenglück, B., Gilman, J., Kuster,
010   W., and de Gouw, J.: Modeling the formation and aging of secondary organic aerosols in Los Angeles during CalNex 2010,
011   Atmospheric Chemistry and Physics, 15, 5773-5801, 2015.

012   Hildebrandt, L., Donahue, N., and Pandis, S.: High formation of secondary organic aerosol from the photo-oxidation
013   of toluene, Atmospheric Chemistry and Physics, 9, 2973-2986, doi:10.5194/acp-9-2973-2009, 2009.

014   Hodzic, A., Jimenez, J., Madronich, S., Canagaratna, M., DeCarlo, P., Kleinman, L., and Fast, J.: Modeling organic
015   aerosols in a megacity: potential contribution of semi-volatile and intermediate volatility primary organic compounds to
016   secondary organic aerosol formation, Atmospheric Chemistry and Physics, 10, 5491-5514, doi:10.5194/acp-10-5491-2010,
017   2010.

018   Huffman, J., Docherty, K., Mohr, C., Cubison, M., Ulbrich, I., Ziemann, P., Onasch, T., and Jimenez, J.: Chemically-
019   resolved volatility measurements of organic aerosol from different sources, Environ. Sci. Technol., 43, 5351-5357, 2009.

020   Jathar, S., Farina, S., Robinson, A., and Adams, P.: The influence of semi-volatile and reactive primary emissions on
021   the abundance and properties of global organic aerosol, Atmospheric Chemistry and Physics, 11, 7727-7746, doi:10.5194/acp-
022   11-7727-2011 2011.

023   Jathar, S. H., Donahue, N. M., Adams, P. J., and Robinson, A. L.: Testing secondary organic aerosol models using
024   smog chamber data for complex precursor mixtures: influence of precursor volatility and molecular structure, Atmospheric

025   Chemistry and Physics, 14, 5771-5780, 2014a.

026   Jathar, S. H., Gordon, T. D., Hennigan, C. J., Pye, H. O. T., Pouliot, G. A., Adams, P. J., Donahue, N. M., and

027   Robinson, A. L.: Unspeciated organic emissions from combustion sources and their influence on the secondary organic aerosol

028   budget in the United States, Proceedings of the National Academy of Sciences, 111, 10473-10478, 2014b.

029   Jathar, S. H., Cappa, C. D., Wexler, A. S., Seinfeld, J. H., and Kleeman, M. J.: Multi-generational oxidation model to

030   simulate secondary organic aerosol in a 3-D air quality model, Geosci. Model Dev., 8, 2553-2567, 10.5194/gmd-8-2553-2015,

031   2015.

032   Jathar, S. H., Cappa, C. D., Wexler, A. S., Seinfeld, J. H., and Kleeman, M. J.: Simulating secondary organic aerosol

033   in a regional air quality model using the statistical oxidation model – Part 1: Assessing the influence of constrained multi-

034   generational ageing, Atmospheric Chemistry & Physics, 16, 2309-2322, 2016.

035   Jathar, S. H., Friedman, B., Galang, A. A., Link, M. F., Brophy, P., Volckens, J., Eluri, S., and Farmer, D. K.: Linking

036   Load, Fuel and Emission Controls to Photochemical Production of Secondary Organic Aerosol from a Diesel Engine, Environ.

037   Sci. Technol., 2017a.

038   Jathar, S. H., Woody, M., Pye, H. O., Baker, K. R., and Robinson, A. L.: Chemical transport model simulations of

039   organic aerosol in southern California: model evaluation and gasoline and diesel source contributions, Atmospheric Chemistry

040   and Physics, 17, 4305-4318, 2017b.

041   Karnezi, E., Riipinen, I., and Pandis, S.: Measuring the atmospheric organic aerosol volatility distribution: a

042   theoretical analysis, Atmospheric Measurement Techniques, 7, 2953-2965, 2014.

043   Konovalov, I. B., Beekmann, M., Berezin, E. V., Petetin, H., Mielonen, T., Kuznetsova, I. N., and Andreae, M. O.:

044   The role of semi-volatile organic compounds in the mesoscale evolution of biomass burning aerosol: a modelling case study of

045   the 2010 mega-fire event in Russia, Atmospheric Chemistry and Physics Discussions, 15, 9107-9172, 2015.

046   Krechmer, J. E., Pagonis, D., Ziemann, P. J., and Jimenez, J. L. L.: Quantification of gas-wall partitioning in Teflon

047   environmental chambers using rapid bursts of low-volatility oxidized species generated in-situ, Environ. Sci. Technol., 2016.

048   Krechmer, J. E., Day, D. A., Ziemann, P. J., and Jimenez, J. L.: Direct measurements of gas/particle partitioning and

049   mass accommodation coefficients in environmental chambers, Environ. Sci. Technol., 51, 11867-11875, 2017.

050   Kroll, J. H., Smith, J. D., Che, D. L., Kessler, S. H., Worsnop, D. R., and Wilson, K. R.: Measurement of

051   fragmentation and functionalization pathways in the heterogeneous oxidation of oxidized organic aerosol, Physical Chemistry

052   Chemical Physics, 11, 8005-8014, 2009.

053   Lambe, A., Chhabra, P., Onasch, T., Brune, W., Hunter, J., Kroll, J., Cummings, M., Brogan, J., Parmar, Y., and

054   Worsnop, D.: Effect of oxidant concentration, exposure time, and seed particles on secondary organic aerosol chemical

055   composition and yield, Atmospheric Chemistry and Physics, 15, 3063-3075, 2015.

056   Lambe, A. T., Ahern, A. T., Williams, L. R., Slowik, J. G., Wong, J. P. S., Abbatt, J. P. D., Brune, W. H., Ng, N. L.,

057   Wright, J. P., and Croasdale, D. R.: Characterization of aerosol photooxidation flow reactors: heterogeneous oxidation,

058   secondary organic aerosol formation and cloud condensation nuclei activity measurements, Atmospheric Measurement

059   Techniques, 4, 445-461, 2011.

060   Lambe, A. T., Onasch, T. B., Croasdale, D. R., Wright, J. P., Martin, A. T., Franklin, J. P., Massoli, P., Kroll, J. H.,

061   Canagaratna, M. R., and Brune, W. H.: Transitions from functionalization to fragmentation reactions of laboratory secondary

062   organic aerosol (SOA) generated from the OH oxidation of alkane precursors, Environ. Sci. Technol., 46, 5430-5437, 2012.

063   Lee, B.-H., Pierce, J. R., Engelhart, G. J., and Pandis, S. N.: Volatility of secondary organic aerosol from the

064   ozonolysis of monoterpenes, Atmospheric environment, 45, 2443-2452, 2011.

065   Lim, Y. B., and Ziemann, P. J.: Effects of molecular structure on aerosol yields from OH radical-initiated reactions of
066   linear, branched, and cyclic alkanes in the presence of NO x, Environ. Sci. Technol., 43, 2328-2334, 2009.

067   Link, M., Friedman, B., Fulgham, R., Brophy, P., Galang, A., Jathar, S., Veres, P., Roberts, J., and Farmer, D.:
068   Photochemical processing of diesel fuel emissions as a large secondary source of isocyanic acid (HNCO), Geophysical
069   Research Letters, 43, 4033-4041, 2016.

070   May, A. A., Levin, E. J. T., Hennigan, C. J., Riipinen, I., Lee, T., Collett, J. L., Jimenez, J. L., Kreidenweis, S. M., and
071   Robinson, A. L.: Gas-particle partitioning of primary organic aerosol emissions: 3. Biomass burning, Journal of Geophysical
072   Research: Atmospheres, 118, 2013JD020286, 10.1002/jgrd.50828, 2013a.

073   May, A. A., Presto, A. A., Hennigan, C. J., Nguyen, N. T., Gordon, T. D., and Robinson, A. L.: Gas-particle
074   partitioning of primary organic aerosol emissions: (2) Diesel vehicles, Environ. Sci. Technol., 47, 8288-8296, 2013b.

075   May, A. A., Presto, A. A., Hennigan, C. J., Nguyen, N. T., Gordon, T. D., and Robinson, A. L.: Gas-particle
076   partitioning of primary organic aerosol emissions: (1) gasoline vehicle exhaust, Atmospheric Environment, 77, 128-139,
077   2013c.

078   Murphy, B., and Pandis, S.: Simulating the formation of semivolatile primary and secondary organic aerosol in a
079   regional chemical transport model., Environ. Sci. Technol., 43, 4722-4728, doi:10.1021/es803168a, 2009.

080   Ng, N., Kroll, J., Chan, A., Chhabra, P., Flagan, R., and Seinfeld, J.: Secondary organic aerosol formation from m-
081   xylene, toluene, and benzene, Atmos. Chem. Phys, 7, 3909-3922, doi:10.5194/acp-7-3909-2007, 2007.

082   Odum, J. R., Hoffmann, T., Bowman, F., Collins, D., Flagan, R. C., and Seinfeld, J. H.: Gas/particle partitioning and
083   secondary organic aerosol yields, Environ. Sci. Technol., 30, 2580-2585, 1996.

084   Ortega, A. M., Hayes, P. L., Peng, Z., Palm, B. B., Hu, W., Day, D. A., Li, R., Cubison, M. J., Brune, W. H., and
085   Graus, M.: Real-time measurements of secondary organic aerosol formation and aging from ambient air in an oxidation flow
086   reactor in the Los Angeles area, Atmospheric Chemistry and Physics, 16, 7411-7433, 2016.

087   Pachauri, R. K., Allen, M. R., Barros, V. R., Broome, J., Cramer, W., Christ, R., Church, J. A., Clarke, L., Dahe, Q.,
088   Dasgupta, P., Dubash, N. K., Edenhofer, O., Elgizouli, I., Field, C. B., Forster, P., Friedlingstein, P., Fuglestvedt, J., Gomez-
089   Echeverri, L., Hallegatte, S., Hegerl, G., Howden, M., Jiang, K., Jimenez Cisneroz, B., Kattsov, V., Lee, H., Mach, K. J.,
090   Marotzke, J., Mastrandrea, M. D., Meyer, L., Minx, J., Mulugetta, Y., O'Brien, K., Oppenheimer, M., Pereira, J. J., Pichs-
091   Madruga, R., Plattner, G. K., Pörtner, H.-O., Power, S. B., Preston, B., Ravindranath, N. H., Reisinger, A., Riahi, K.,
092   Rusticucci, M., Scholes, R., Seyboth, K., Sokona, Y., Stavins, R., Stocker, T. F., Tschakert, P., van Vuuren, D., and van
093   Ypserle, J. P.: Climate Change 2014: Synthesis Report. Contribution of Working Groups I, II and III to the Fifth Assessment
094   Report of the Intergovernmental Panel on Climate Change, edited by: Pachauri, R. K., and Meyer, L., IPCC, Geneva,
095   Switzerland, 151 pp., 2014.

096   Palm, B. B., Campuzano-Jost, P., Ortega, A. M., Day, D. A., Kaser, L., Jud, W., Karl, T., Hansel, A., Hunter, J. F.,
097   and Cross, E. S.: In situ secondary organic aerosol formation from ambient pine forest air using an oxidation flow reactor,
098   Atmospheric Chemistry and Physics, 16, 2943-2970, 2016.

099   Pankow, J. F.: An absorption model of gas/particle partitioning of organic compounds in the atmosphere, Atmospheric
100   Environment, 28, 185-188, 1994.

101   Pankow, J. F., and Barsanti, K. C.: The carbon number-polarity grid: A means to manage the complexity of the mix of
102   organic compounds when modeling atmospheric organic particulate matter, Atmospheric Environment, 43, 2829-2835, 2009.

103   Peng, Z., Day, D., Stark, H., Li, R., Lee-Taylor, J., Palm, B., Brune, W., and Jimenez, J.: HOx radical chemistry in

104   oxidation flow reactors with low-pressure mercury lamps systematically examined by modeling, Atmospheric Measurement

105   Techniques, 8, 4863-4890, 2015.

106   Presto, A. A., Miracolo, M. A., Donahue, N. M., and Robinson, A. L.: Secondary organic aerosol formation from

107   high-NO x photo-oxidation of low volatility precursors: n-alkanes, Environ. Sci. Technol., 44, 2029-2034, 2010.

108   Presto, A. A., Nguyen, N. T., Ranjan, M., Reeder, A. J., Lipsky, E. M., Hennigan, C. J., Miracolo, M. A., Riemer, D.

109   D., and Robinson, A. L.: Fine particle and organic vapor emissions from staged tests of an in-use aircraft engine, Atmospheric

110   Environment, 45, 3603-3612, 2011.

111   Pye, H., and Seinfeld, J.: A global perspective on aerosol from low-volatility organic compounds, Atmos. Chem.

112   Phys, 10, 4377-4401, doi:10.5194/acp-10-4377-2010, 2010.

113   Robinson, A. L., Donahue, N. M., Shrivastava, M. K., Weitkamp, E. A., Sage, A. M., Grieshop, A. P., Lane, T. E.,

114   Pierce, J. R., and Pandis, S. N.: Rethinking organic aerosols: Semivolatile emissions and photochemical aging, Science, 315,

115   1259-1262, 2007.

116   Saleh, R., Donahue, N. M., and Robinson, A. L.: Time scales for gas-particle partitioning equilibration of secondary

117   organic aerosol formed from alpha-pinene ozonolysis, Environ. Sci. Technol., 47, 5588-5594, 2013.

118   Seinfeld, J. H., and Pandis, S. N.: Atmospheric Chemistry and Physics, John Wiley and Sons., New York, 2006.

119   Simonen, P., Saukko, E., Karjalainen, P., Timonen, H., Bloss, M., Aakko-Saksa, P., Rönkkö, T., Keskinen, J., and Dal

120   Maso, M.: A new oxidation flow reactor for measuring secondary aerosol formation of rapidly changing emission sources,

121   Atmospheric Measurement Techniques, 10, 1519, 2017.

122   Song, C., Na, K., Warren, B., Malloy, Q., and Cocker III, D. R.: Secondary organic aerosol formation from the

123   photooxidation of p-and o-xylene, Environ. Sci. Technol., 41, 7403-7408, 2007.

124   Tkacik, D. S., Presto, A. A., Donahue, N. M., and Robinson, A. L.: Secondary organic aerosol formation from

125   intermediate-volatility organic compounds: cyclic, linear, and branched alkanes, Environ. Sci. Technol., 46, 8773-8781, doi:

126   10.1021/es301112c, 2012.

127   Tkacik, D. S., Lambe, A. T., Jathar, S., Li, X., Presto, A. A., Zhao, Y., Blake, D., Meinardi, S., Jayne, J. T., Croteau,

128   P. L., and Robinson, A. L.: Secondary Organic Aerosol Formation from in-Use Motor Vehicle Emissions Using a Potential

129   Aerosol Mass Reactor, Environ. Sci. Technol., 48, 11235-11242, 10.1021/es502239v, 2014.

130   Tsimpidi, A., Karydis, V., Zavala, M., Lei, W., Molina, L., Ulbrich, I., Jimenez, J., and Pandis, S.: Evaluation of the

131   volatility basis-set approach for the simulation of organic aerosol formation in the Mexico City metropolitan area, Atmos.

132   Chem. Phys, 10, 525-546, doi:10.5194/acp-10-525-2010, 2009.

133   Zhang, X., Cappa, C. D., Jathar, S. H., McVay, R. C., Ensberg, J. J., Kleeman, M. J., and Seinfeld, J. H.: Influence of

134   vapor wall loss in laboratory chambers on yields of secondary organic aerosol, Proceedings of the National Academy of

135   Sciences, 111, 5802-5807, 2014.

136   Zhao, Y., Nguyen, N. T., Presto, A. A., Hennigan, C. J., May, A. A., and Robinson, A. L.: Intermediate volatility

137   organic compound emissions from on-road diesel vehicles: chemical composition, emission factors, and estimated secondary

138   organic aerosol production, Environ. Sci. Technol., 49, 11516-11526, 2015.

139

7 Tables

Table 1: Primary emissions of THC and POA, maximum photochemical production of SOA, maximum O:C of the OA, maximum OH exposure, and size distribution data from Jathar et al. (2017a).

Load-Fuel-Aftertreatment Experiment	Date	THC ($\mu g\ m^{-3}$)	CO (ppbv)	NO (ppbv)	NO$_2$ (ppbv)	POA ($\mu g\ m^{-3}$)	SOA[%] ($\mu g\ m^{-3}$)	O: C[%]	OH Exposure[%] (molec.-hr cm^{-3})	Number Mean Dia.[*] (nm)	Number Conc.[*] (# cm^{-3})
Idle-Diesel-None	June 3	1519	2746	960	318	38±15	209±66	0.23±0.01	2.1×10^7		8.0×10^5
	June 5	1810	5809	878	502	35±11	875±288	0.46±0.07	6.67×10^7	46	6.5×10^5
	June 12	2554	9664	1870	1103	85±17	877±277	0.57±0.09	3.61×10^7		3.4×10^5
Idle-Biodiesel-None	June 4	1118	4270	867	344	22±12	999±316	0.52±0.07	9.17×10^7	46[@]	$7.3\times10^{5@}$
	June 8	2160	8169	1578	811	69±20	1415±468	0.36±0.03	4.72×10^7		$4.1\times10^{5@}$
Load-Diesel-None	June 3	959	1558	4999	379	19±11	181±58	0.37±0.01	3.6×10^7	190	5.3×10^5
	June 5	711	1400	6690	34	37±13	253±100	0.32±0.04	2.61×10^7		4.4×10^5
Load- Biodiesel-None	June 4	1634	1410	6364	30	29±18	645±204	0.38±0.05	2.78×10^7	190[@]	$5.0\times10^{5@}$
	June 8	518	2051	10813	496	46±22	284±106	0.30±0.04	1.42×10^7		$3.3\times10^{5@}$
Idle-Diesel-DPF+DOC	June 9	2135	7473	2383	23	1.5±0.6	1040±335	0.37±0.02	5×10^7	52	910
Load-Diesel-DPF+DOC	June 9	303	85	6157	4483	1.6±3.6	146±48	0.29±0.01	1.31×10^7	57	968
Idle-Biodiesel-DPF+DOC	June 10	1773	7452	2213	182	2.6±1	787±250	0.44±0.04	5.28×10^7	52[@]	910[@]
Load-Biodiesel-DPF+DOC	June 10	261	58	5475	4525	2±0.14	107±9	0.29±0.01	1.39×10^7	57[@]	968[@]

DPF=diesel particulate filter, DOC=diesel oxidation catalyst

[%]maximum values measured in each experiment

[*]values measured at no OH exposure

[@]No data, assumed to be similar to the equivalent diesel experiment for the model

Table 2: SOA precursors and mass yields used in the VBS model for high NO$_X$ conditions.

Species	$log_{10}C^*$					Reference
	0.1	1	10	100	1000	
toluene	0.0000	0.0100	0.2400	0.4500	0.7000	Hildebrandt et al. (2009)
benzene	0.0392	0.0315	0.0000	0.8230	0.0957	Ng et al. (2007)[#]
m-xylene	0.0032	0.0106	0.0633	0.0465	0.0000	Ng et al. (2007)[#]
p-xylene	0.0000	0.0022	0.0764	0.0000	0.0000	Song et al. (2007)[#]
o-xylene	0.0000	0.0132	0.1140	0.0000	0.0000	Song et al. (2007)[#]
naphthalene	0.0000	0.1660	0.0000	0.5400	0.8130	Chan et al. (2009)[#]
1-methylnaphthalene	0.0000	0.0170	0.4860	0.0000	0.0000	Chan et al. (2009)[#]
2-methylnaphthalene	0.0000	0.0531	0.5040	0.0000	0.0000	Chan et al. (2009)[#]
1,2-dimethylnaphthalene	0.0000	0.3100	0.0000	0.0000	0.0000	Chan et al. (2009)[#]
1-methyl-3-n-propylbenzene	0.0000	0.0000	0.0405	0.0694	0.1140	Odum et al. (1996)[#]
n-decane	0.0000	0.0000	0.0110	0.1280	0.2420	Presto et al. (2010)[&]
n-undecane	0.0000	0.0040	0.0720	0.1760	0.1450	Presto et al. (2010)[&]
n-dodecane	0.0000	0.0140	0.1100	0.1600	0.0000	Presto et al. (2010)[&]
n-tridecane	0.0140	0.0590	0.0940	0.0710	0.0000	Presto et al. (2010)[&]
n-tetradecane	0.0940	0.3000	0.3500	0.0000	0.0000	Presto et al. (2010)[&]
n-pentadecane	0.0440	0.0710	0.4100	0.3000	0.0000	Presto et al. (2010)[&]
n-hexadecane	0.0530	0.0830	0.4600	0.2500	0.0000	Presto et al. (2010)[&]
n-heptadecane	0.0630	0.0890	0.5500	0.2000	0.0000	Presto et al. (2010)[&]
n-octadecane	0.0760	0.3195	0.3750	0.1000	0.0000	Presto et al. (2010)[&]
n-nonadecane	0.0890	0.5500	0.2000	0.0000	0.0000	Presto et al. (2010)[&]
n-eicosane	0.3195	0.3750	0.1000	0.0000	0.0000	Presto et al. (2010)[&]
n-heneicosane	0.5500	0.2000	0.0000	0.0000	0.0000	Presto et al. (2010)[&]
n-docosane	0.3750	0.1000	0.0000	0.0000	0.0000	Presto et al. (2010)[&]

[&]extrapolated from the Presto et al. (2010) data

[#]do not account for vapor wall losses

Table 3: SOA precursors and mass yields used in the VBS model for low NO$_X$ conditions.

Species	C^*					Reference
	0.1	1	10	100	1000	
toluene	0.0000	0.0100	0.2400	0.7000	0.7000	Hildebrandt et al. (2009)
benzene	0.0000	0.0000	0.0000	0.3700	0.0000	Ng et al. (2007)[#]
m-xylene	0.0000	0.0000	0.0000	0.0310	0.0000	Ng et al. (2007)[#]
p-xylene	0.0000	0.0000	0.0000	0.0310	0.0000	Ng et al. (2007)[#]
o-xylene	0.0000	0.0000	0.0000	0.0310	0.0000	Ng et al. (2007)[#]
naphthalene	0.0000	0.1565	0.0000	0.1199	0.2708	Chan et al. (2009)[#]
1-methylnaphthalene	0.0000	0.1565	0.0000	0.1199	0.2708	Chan et al. (2009)[#]
2-methylnaphthalene	0.0000	0.1565	0.0000	0.1199	0.2708	Chan et al. (2009)[#]
n-decane	0.0002	0.0050	0.0013	0.3938	0.0278	Loza et al. (2014)[&]
n-undecane	0.0001	0.0070	0.0216	0.3321	0.0000	Loza et al. (2014)[&]
n-dodecane	0.0011	0.0080	0.0279	0.3902	0.0003	Loza et al. (2014)[&]
n-tridecane	0.0029	0.0064	0.0551	0.3231	0.7090	Loza et al. (2014)[&]
n-tetradecane	0.0004	1.2000	0.1777	0.0194	0.0014	Loza et al. (2014)[&]
n-pentadecane	0.0032	0.0124	0.0686	0.5050	0.0025	Loza et al. (2014)[&]

n-hexadecane	0.0000	0.0572	0.2754	0.4346	0.1710	Loza et al. (2014)[&]
n-heptadecane	0.0399	0.0757	0.4409	0.3691	0.0000	Loza et al. (2014)[&]
n-octadecane	0.1958	0.0203	0.7077	0.0777	0.0000	Loza et al. (2014)[&]
n-nonadecane	1.0281	0.0000	0.0000	0.0000	0.0000	Loza et al. (2014)[&]
n-eicosane	0.0024	0.8470	0.2160	0.0000	0.0000	Loza et al. (2014)[&]
n-heneicosane	0.3629	0.6766	0.0250	0.0000	0.0000	Loza et al. (2014)[&]
n-docosane	0.7991	0.2633	0.0000	0.0000	0.0000	Loza et al. (2014)[&]
C_{12} branched alkane	0.0077	0.0015	0.0416	0.2486	0.9179	Loza et al. (2014)[&]
C_{13} branched alkane	0.0105	0.0007	0.0610	0.2376	1.2045	Loza et al. (2014)[&]
C_{14} branched alkane	0.0135	0.0007	0.0819	0.4173	0.4879	Loza et al. (2014)[&]
C_{15} branched alkane	0.0156	0.0034	0.1677	0.3553	0.7973	Loza et al. (2014)[&]
C_{16} branched alkane	0.0075	0.0704	0.1689	0.5741	0.0000	Loza et al. (2014)[&]
C_{17} branched alkane	0.0510	0.0000	0.4527	0.4605	0.0000	Loza et al. (2014)[&]
C_{18} branched alkane	0.0836	0.0001	0.7962	0.1484	0.0000	Loza et al. (2014)[&]
C_{19} branched alkane	0.3151	0.0001	0.7470	0.0000	0.0000	Loza et al. (2014)[&]
C_{20} branched alkane	0.0198	0.8698	0.1725	0.0000	0.0000	Loza et al. (2014)[&]
C_{21} branched alkane	0.3753	0.6837	0.0000	0.0000	0.0000	Loza et al. (2014)[&]
C_{22} branched alkane	0.8517	0.2056	0.0000	0.0000	0.0000	Loza et al. (2014)[&]
C_{12} cyclic alkane	0.0128	0.0302	0.0124	0.6156	0.0043	Loza et al. (2014)[&]
C_{13} cyclic alkane	0.0297	0.0000	0.0939	0.4062	1.0776	Loza et al. (2014)[&]
C_{14} cyclic alkane	0.0322	0.0000	0.1521	0.5341	0.5717	Loza et al. (2014)[&]
C_{15} cyclic alkane	0.0345	0.0000	0.3430	0.3231	0.8672	Loza et al. (2014)[&]
C_{16} cyclic alkane	0.0147	0.1426	0.3616	0.2839	0.6597	Loza et al. (2014)[&]
C_{17} cyclic alkane	0.0574	0.2408	0.3453	0.4060	0.0000	Loza et al. (2014)[&]
C_{18} cyclic alkane	0.2546	0.0643	0.6091	0.1431	0.0000	Loza et al. (2014)[&]
C_{19} cyclic alkane	0.2940	0.2790	0.5010	0.0000	0.0000	Loza et al. (2014)[&]
C_{20} cyclic alkane	0.3423	0.5700	0.1653	0.0000	0.0000	Loza et al. (2014)[&]
C_{21} cyclic alkane	0.6100	0.4478	0.0155	0.0000	0.0000	Loza et al. (2014)[&]
C_{22} cyclic alkane	0.9573	0.1110	0.0013	0.0000	0.0000	Loza et al. (2014)[&]

[&]produced from pseudo chamber data generated using the SOM
[#]do not account for vapor wall losses

Table 4: SOA precursors and parameters used in the SOM (Cappa et al., 2016) for high NO_X conditions.

Species	m_{frag}	ΔLVP	$p_{O,1}$	$p_{O,2}$	$p_{O,3}$	$p_{O,4}$	Reference
n-dodecane	0.0980	1.3900	0.9270	0.0101	0.0180	0.0445	Loza et al. (2014)
methylundecane	0.0100	1.2100	0.7419	0.0011	0.1820	0.0750	Loza et al. (2014)
hexylcyclohexane	0.0477	1.5700	0.7313	0.0381	0.2101	0.0205	Loza et al. (2014)
toluene	0.2220	1.2400	0.0029	0.0010	0.0010	1.0100	Zhang et al. (2014)
benzene	0.5350	1.7000	0.0792	0.0010	0.9190	0.0010	Ng et al. (2007)
m-xylene	0.0100	1.6800	0.9360	0.0010	0.0021	0.0609	Ng et al. (2007)
naphthalene	0.1210	1.3100	0.6440	0.0010	0.0460	0.3080	Chan et al. (2009)

Table 5: SOA precursors and parameters used in the SOM (Cappa et al., 2016) for low NO_X conditions.

Species	m_{frag}	ΔLVP	$p_{O,1}$	$p_{O,2}$	$p_{O,3}$	$p_{O,4}$	Reference
n-dodecane	2.0000	1.8300	0.9990	0.0010	0.0010	0.0010	Loza et al. (2014)

methylundecane	2.8200	1.9100	0.9980	0.0010	0.0010	0.0010	Loza et al. (2014)
hexylcyclohexane	5.0000	2.0500	0.8160	0.1810	0.0019	0.0010	Loza et al. (2014)
toluene	1.3100	1.7700	0.1850	0.0010	0.0019	0.8120	Zhang et al. (2014)
benzene	0.0807	1.9700	0.6370	0.0010	0.0021	0.3600	Ng et al. (2007)
m-xylene	1.0800	2.0500	0.1020	0.0010	0.8780	0.0190	Ng et al. (2007)
naphthalene	0.1890	1.8700	0.3520	0.0543	0.5330	0.0609	Chan et al. (2009)

Table 6: (a) Volatility- and (b) carbon-number resolved distributions used to determine mass concentrations of POC in the VBS and SOM models respectively. The volatility distributions are from (May et al., 2013b)..

C^* ($\mu g\ m^{-3}$)	10^{-2}	10^{-1}	10^{1}	10^{2}	10^{3}	10^{4}	10^{5}	10^{6}
f_i	0.03	0.25	0.37	0.23	0.06	0.03	0.01	0.01

Carbon No.	<16	16	17	18	19	20	21	22	23	24	25	26	>26
f_i	0.003	0.000	0.058	0.043	0.055	0.094	0.146	0.181	0.178	0.137	0.078	0.026	0.001

Table 7: Reaction rate constants (k_{OH}), mass fractions, and VBS and SOM surrogates for SOA precursors in diesel and biodiesel emissions. k_{OH} values are from Atkinson and Arey (2003) when available or the EPI Suite version 4.11 (EPA, 2017).

Species	Carbon Number	k_{OH} (cm^3 molecules^{-1} s^{-1})	Mass Percentage of THC		VBS Surrogate	SOM Surrogate
			Diesel	Biodiesel		
ethylbenzene	8	7.0×10^{-12}	0.2516	0.0826	toluene	toluene
indan	9	1.9×10^{-11}	0.1542	NA	naphthalene	naphthalene
butylbenzene	10	4.5×10^{-12}	0.0081	0.4720	*m*-xylene	*m*-xylene
diethylbenzene	10	8.11×10^{-12}	0.0731	NA	*m*-xylene	*m*-xylene
isopropyltoluene	10	8.54×10^{-12}	NA	0.3599	toluene	toluene
m-xylene	8	2.31×10^{-11}	0.4951	0.3717	*m*-xylene	*m*-xylene
o-xylene	8	1.36×10^{-11}	0.2760	0.3953	*o*-xylene	*m*-xylene
p-xylene	8	1.43×10^{-11}	0.0812	NA	*p*-xylene	*m*-xylene
n-decane	10	1.1×10^{-11}	0.4302	1.7050	*n*-decane	*n*-decane
n-undecane	11	1.23×10^{-11}	0.2110	1.9410	*n*-undecane	*n*-dodecane
toluene	7	5.63×10^{-12}	1.1932	1.6401	toluene	toluene
n-tridecane	13	1.68×10^{-11}	NA	0.6136	*n*-tridecane	*n*-dodecane
benzaldehyde	7	1.2×10^{-11}	0.5682	NA	benzene	benzene
benzene	6	1.22×10^{-12}	1.6234	1.5988	benzene	benzene
C_{10} aromatics	10	2.3×10^{-11}	0.0649	NA	*m*-xylene	*m*-xylene
C_9 aromatics	9	2.31×10^{-11}	0.4058	NA	*m*-xylene	*m*-xylene
1,2,3-trimethylbenzene	9	3.27×10^{-11}	0.0974	NA	*m*-xylene	*m*-xylene
1,2,4-trimethylbenzene	9	3.25×10^{-11}	0.4302	0.4720	*m*-xylene	*m*-xylene

1,2-diethylbenzene	10	8.11×10^{-12}	0.0731	NA	toluene	toluene
1,3,5-trimethylbenzene	9	5.67×10^{-11}	NA	0.1888	*m*-xylene	*m*-xylene
1,2-dimethyl-4-ethylbenzene	10	1.69×10^{-11}	NA	0.176	*m*-xylene	*m*-xylene
1,3-dimethyl-2-ethylbenzene	10	1.76×10^{-11}	NA	0.3304	*m*-xylene	*m*-xylene
1,4-dimethyl-2-ethylbenzene	10	1.69×10^{-11}	NA	0.4366	*m*-xylene	*m*-xylene
1-(1,1-dimethylethyl)-3,5-dimethylbenzene	12	3.01×10^{-11}	NA	0.3717	*m*-xylene	*m*-xylene
1-methyl-2-ethylbenzene	9	7.44×10^{-12}	0.1136	0.3835	toluene	toluene
1-methyl-3-ethylbenzene	9	1.39×10^{-11}	0.2029	0.7198	toluene	toluene
1-methyl-2-tert-butylbenzene	11	6.74×10^{-12}	NA	0.4307	toluene	toluene
1-tert-butyl-4-ethylbenzene	12	7.42×10^{-12}	NA	0.1947	*m*-xylene	*m*-xylene
2-methyl-butyl-benzene	11	1.02×10^{-11}	NA	1.1032	*m*-xylene	*m*-xylene
3,3-dimethyloctane	10	7.21×10^{-12}	NA	0.3068	*n*-decane	methylundecane
3-ethyloctane	10	1.18×10^{-11}	NA	0.1888	*n*-decane	methylundecane
3-methylnonane	10	1.14×10^{-11}	NA	0.2655	*n*-decane	methylundecane
C_{12} branched alkane	12	1.82×10^{-11}	1.1335	1.1335	*n*-decane	methylundecane
C_{13} branched alkane	13	1.68×10^{-11}	0.8111	0.8111	*n*-undecane	methylundecane
C_{14} branched alkane	14	1.39×10^{-11}	0.5257	0.5257	*n*-dodecane	methylundecane
C_{15} branched alkane	15	1.82×10^{-11}	0.4692	0.4692	*n*-tridecane	methylundecane
C_{16} branched alkane	16	1.96×10^{-11}	0.4935	0.4935	*n*-tetradecane	methylundecane
C_{17} branched alkane	17	2.1×10^{-11}	0.2198	0.2198	*n*-pentadecane	methylundecane
C_{18} branched alkane	18	2.24×10^{-11}	0.2863	0.2863	*n*-hexadecane	methylundecane
C_{19} branched alkane	19	2.38×10^{-11}	0.1716	0.1716	*n*-heptadecane	methylundecane
C_{20} branched alkane	20	2.52×10^{-11}	0.0969	0.0969	*n*-octadecane	methylundecane
C_{21} branched alkane	21	2.67×10^{-11}	0.0639	0.0639	*n*-nonadecane	methylundecane
C_{22} branched alkane	22	2.81×10^{-11}	0.0604	0.0604	*n*-eicosane	methylundecane
C_{12} cyclic alkane	12	1.82×10^{-11}	4.3427	4.3427	*n*-tetradecane	hexylcyclohexane
C_{13} cyclic alkane	13	1.68×10^{-11}	4.4265	4.4265	*n*-pentadecane	hexylcyclohexane
C_{14} cyclic alkane	14	1.39×10^{-11}	3.1480	3.1480	*n*-hexadecane	hexylcyclohexane
C_{15} cyclic alkane	15	1.82×10^{-11}	2.8599	2.8599	*n*-	hexylcyclohexane

|					heptadecane	
C_{16} cyclic alkane	16	1.96×10^{-11}	2.1848	2.1848	*n*-octatadecane	hexylcyclohexane
C_{17} cyclic alkane	17	2.1×10^{-11}	1.8546	1.8546	*n*-nonadecane	hexylcyclohexane
C_{18} cyclic alkane	18	2.24×10^{-11}	1.6900	1.6900	*n*-eicosane	hexylcyclohexane
C_{19} cyclic alkane	19	2.38×10^{-11}	1.0570	1.0570	*n*-heneicosane	hexylcyclohexane
C_{20} cyclic alkane	20	2.52×10^{-11}	0.5900	0.5900	*n*-docosane	hexylcyclohexane
C_{21} cyclic alkane	21	2.67×10^{-11}	0.3736	0.3736	*n*-tricosane	hexylcyclohexane
C_{22} cyclic alkane	22	2.81×10^{-11}	0.3141	0.3141	*n*-tricosane	hexylcyclohexane
dodecane	12	1.82×10^{-11}	0.5830	0.5830	*n*-dodecane	*n*-dodecane
tridecane	13	1.68×10^{-11}	0.5465	0.5465	*n*-tridecane	*n*-dodecane
tetradecane	14	1.39×10^{-11}	0.3649	0.3649	*n*-tetradecane	*n*-dodecane
pentadecane	15	1.82×10^{-11}	0.3063	0.3063	*n*-pentadecane	*n*-dodecane
hexadecane	16	1.96×10^{-11}	0.2281	0.2281	*n*-hexadecane	*n*-dodecane
heptadecane	17	2.1×10^{-11}	0.1655	0.1655	*n*-heptadecane	*n*-dodecane
octadecane	18	2.24×10^{-11}	0.1481	0.1481	*n*-octatadecane	*n*-dodecane
nonadecane	19	2.38×10^{-11}	0.0726	0.0726	*n*-nonadecane	*n*-dodecane
eicosane	20	2.52×10^{-11}	0.0365	0.0365	*n*-eicosane	*n*-dodecane
heneicosane	21	2.67×10^{-11}	0.0222	0.0222	*n*-heneicosane	*n*-dodecane
docosane	22	2.81×10^{-11}	0.0143	0.0143	*n*-docosane	*n*-dodecane
pristane	19	2.44×10^{-11}	0.1434	0.1434	*n*-nonadecane	methylundecane
phytane	20	2.61×10^{-11}	0.0799	0.0799	*n*-eicosane	methylundecane
naphthalene	10	2.3×10^{-11}	0.1038	0.1038	naphthalene	naphthalene
phenanthrene	14	1.3×10^{-11}	0.0117	0.0117	naphthalene	naphthalene

169
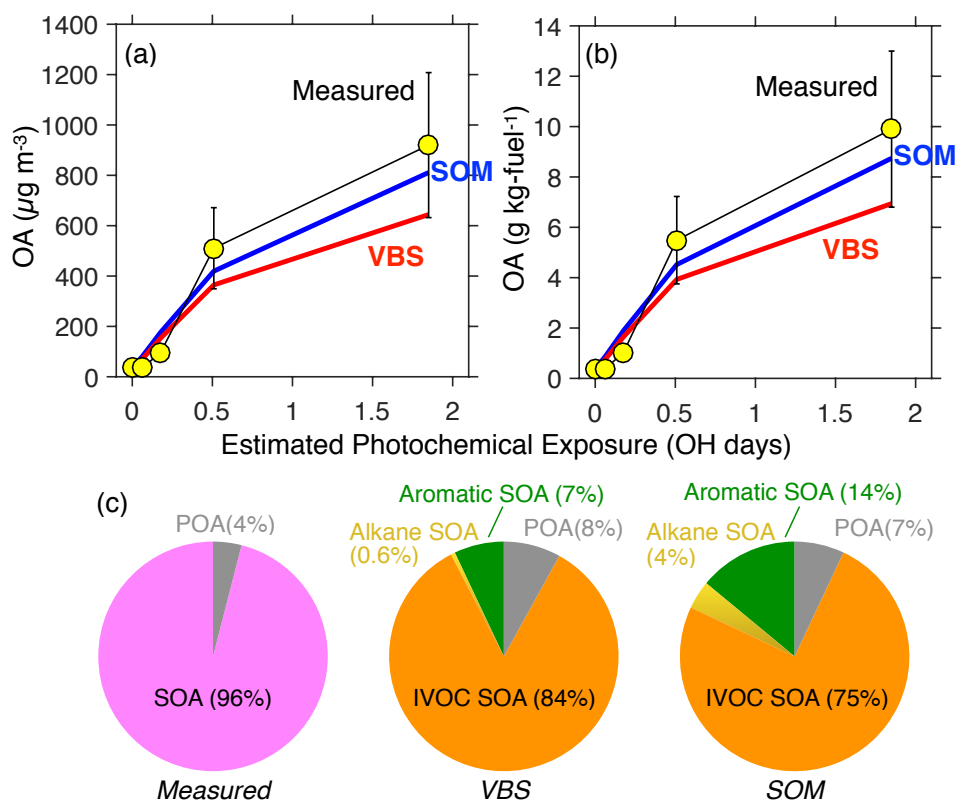
8 Figures

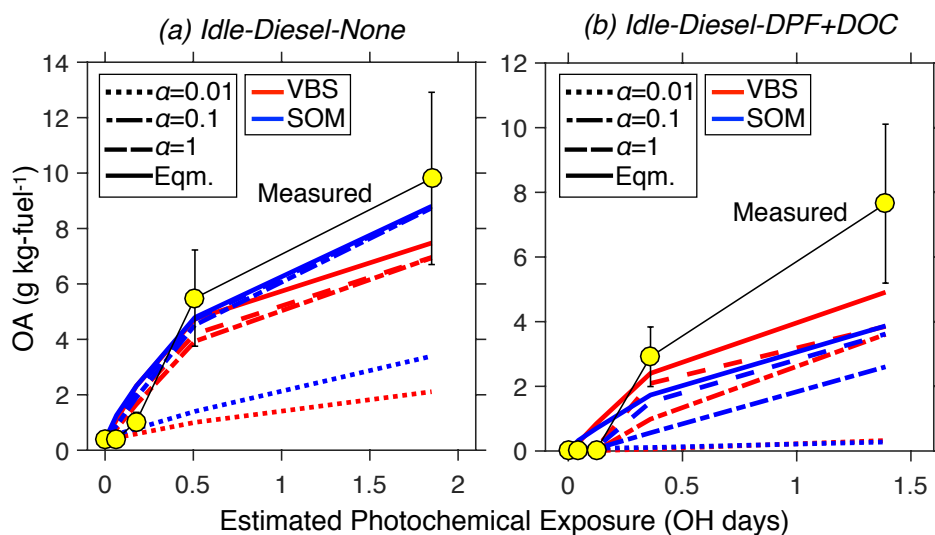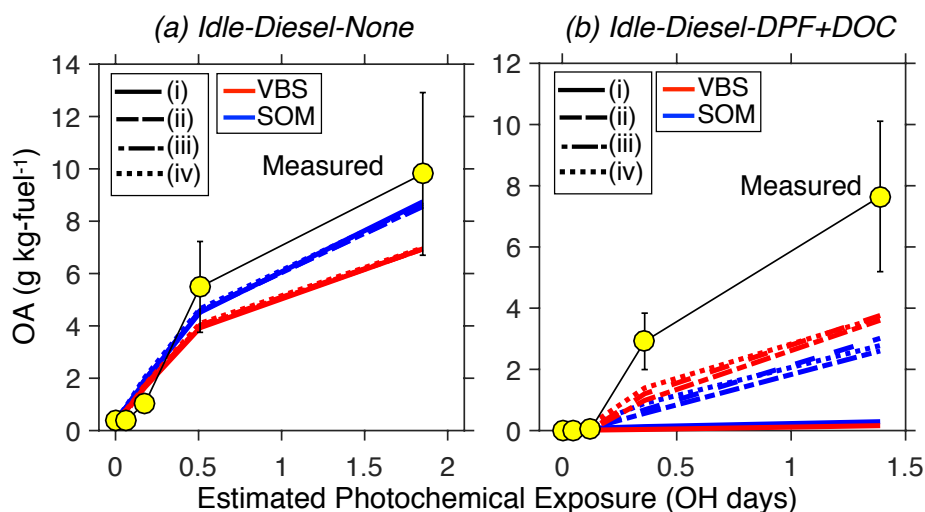*Figure 1: VBS and SOM model predictions of OA compared to measurements from the experiment*
performed on June 5 (Idle-Diesel-None) as a function of photochemical age. Inputs for both models have
been specified in the text. Panel (a) has comparisons in µg m⁻³ and panel (b) has comparisons in g kg-
fuel⁻¹. Panel (c) shows the modeled and measured OA composition at the highest photochemical exposure.

Figure 2: VBS model predictions of OA compared to measurements from the experiment performed on
June 5 (Idle-Diesel-None) as a function of photochemical age assuming instantaneous equilibrium
partitioning and kinetic gas/particle partitioning run at three accommodation coefficients, α = 1 (dash-
dot) ,0.1 (dash) and 0.01 (solid).

184
185 *Figure 3: VBS and SOM model predictions of OA compared to measurements from the experiments*
186 *performed on (a) June 5 (Idle-Diesel-None) and (b) June 11 (Idle-Diesel-DPF+DOC) as a function of*
187 *photochemical age for four different particle size distribution inputs: (i) number mean diameter and*
188 *measured number concentration at no OH exposure (solid), (ii) number mean diameter and measured*
189 *number concentration at the given OH exposure (dash), (iii) average of (i) and (ii) (dash-dot), and (iv)*
190 *nucleation of 1 nm particles (dot).*

191
192
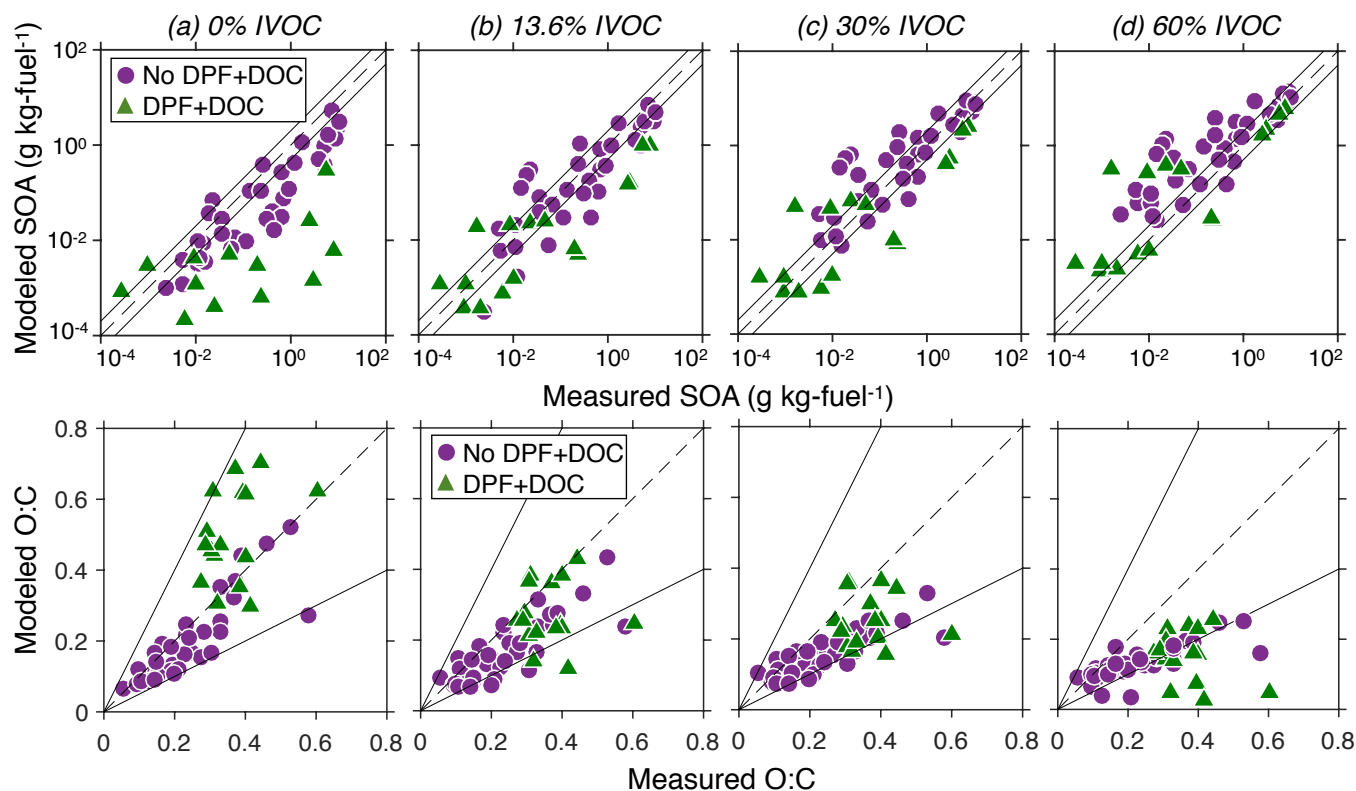
193
194 *Figure 4: Scatter plot comparing SOM predictions of OA mass and O:C to measurements from all*
195 *experiments at all photochemical ages at four different IVOC mass fractions: (a) 0%, (b) 13.76%, (c)*
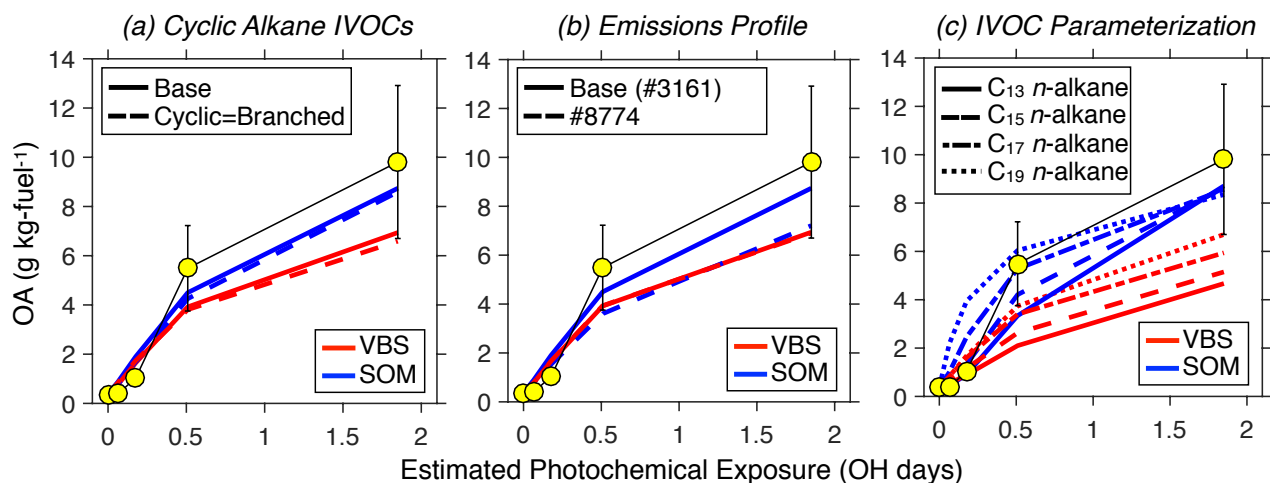196 *30%, and (d) 60%.*
197

7

Figure 5: VBS and SOM predictions of OA compared to measurements from the experiment performed on June 5 (Idle-Diesel-None) as a function of photochemical age. Panel (a) examines uncertainty in model treatment of cyclic alkanes, panel (b) examines uncertainty in the VOC emissions profile, and (c) explores suitability of using a single surrogate linear alkane to model SOA formation from all IVOCs.
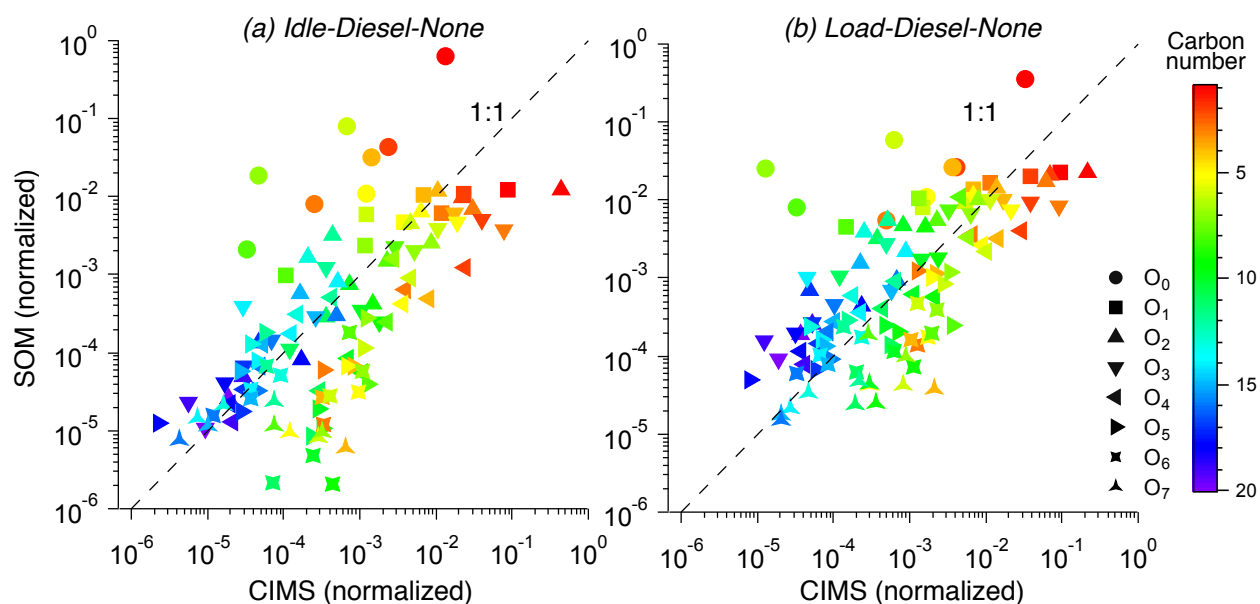

Figure 6: Normalized gas-phase concentration predictions from the SOM model for the Idle-Diesel-None and Load-Diesel-None experiments performed on June 5 and compared to normalized gas-phase concentrations measured by the CIMS.
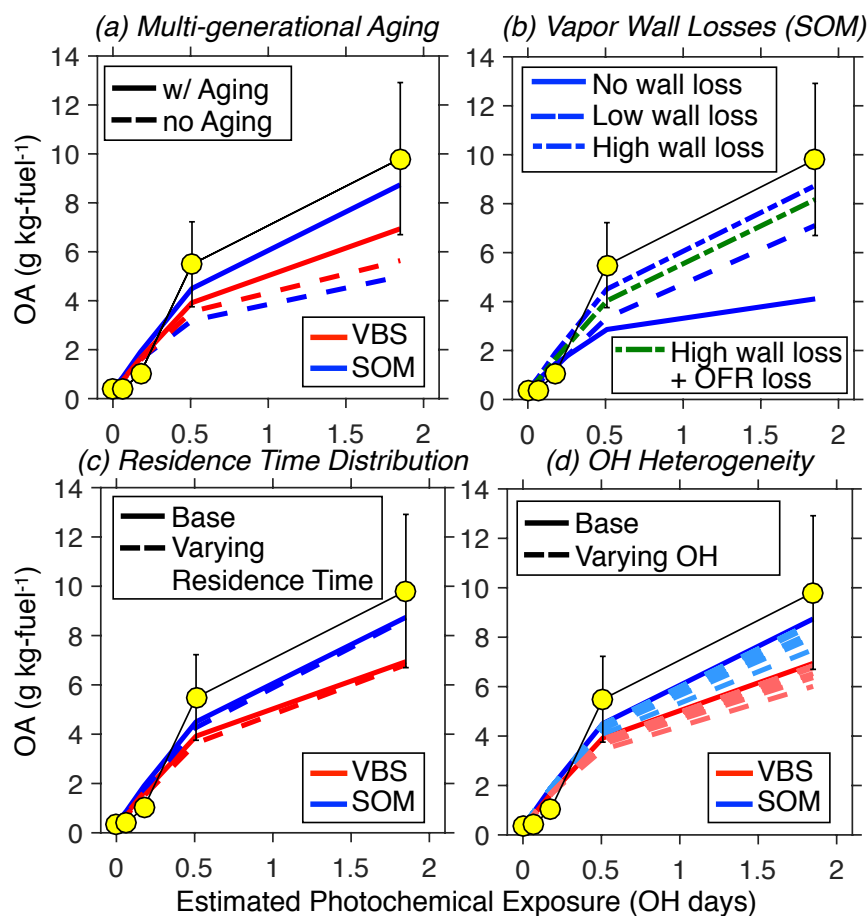
8

Figure 7: VBS and SOM predictions of OA compared to measurements from the experiment performed on June 5 (Idle-Diesel-None) as a function of photochemical age. Panels (a), (b), (c), and (d) examine the influence of multi-generational aging, vapor wall losses, residence time distribution, and spatial heterogeneity in OH concentrations respectively. The dashed lines in panel (d) are deliberately lighter in color than the solid line to help differentiate the Base result from the sensitivity results.
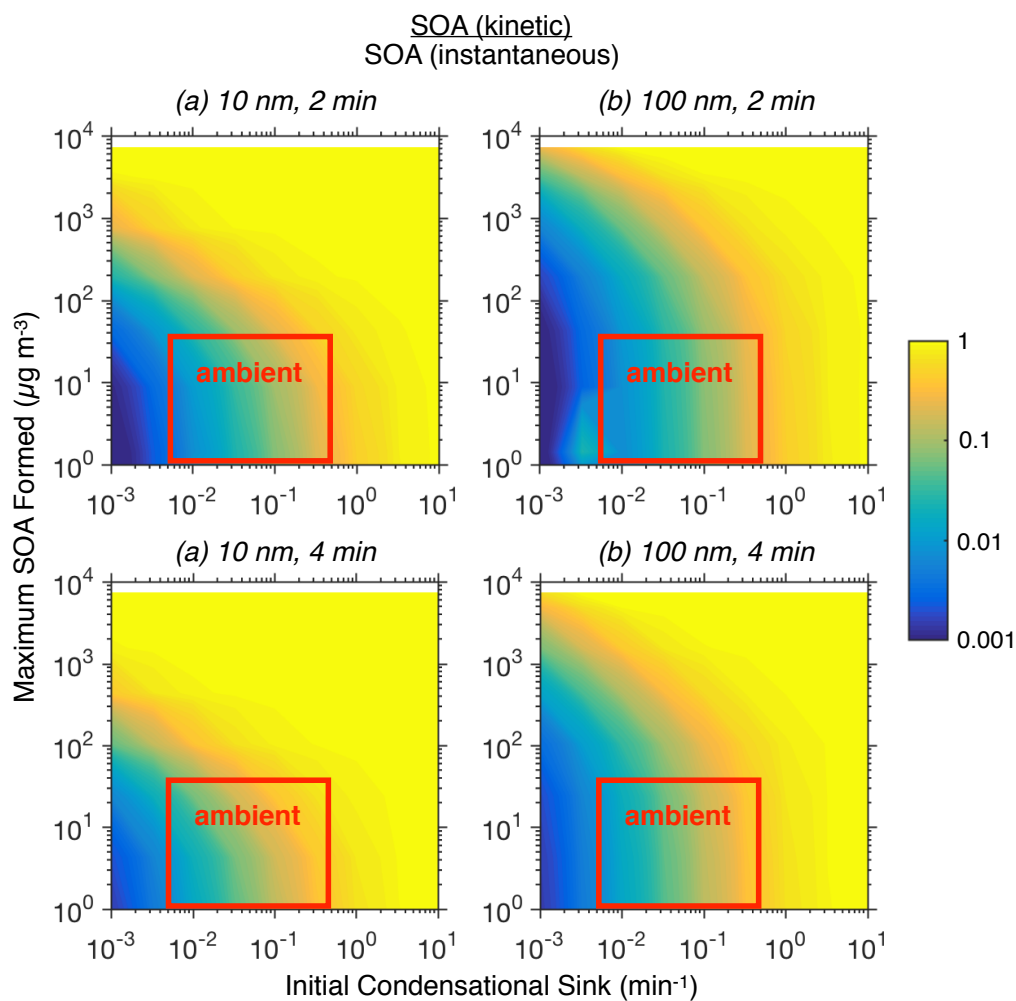
Figure 8: Model predictions of the ratio of SOA produced under kinetic partitioning assumptions to the SOA produced under instantaneous partitioning assumptions as a function of the initial condensational sink and the SOA formed under instantaneous partitioning. Panels are for calculations performed at two different particles sizes: 10 and 100 nm and two different residence times: 2 and 4 min.